TÉCNICO LISBOA

Optimization of CoFeB-AlOx Thin Films for Integration in Advanced Magnetoresistive Devices

MIGUEL SÉRGIO DE ABREU NETO

Thesis to obtain the Master of Science Degree in

MESTRADO EM ENGENHARIA DE MATERIAIS

Supervisors: Prof. Susana Freitas, Filipe Cardoso

Examination Comittee

Chairperson: Prof. Maria de Fátima Reis Vaz
Supervisor: Prof. Susana Freitas
Members of the Committee: Prof. Diana Leitão

Setembro 2014

Agradecimentos

"*A vida de uma pessoa não é o que lhe acontece, mas aquilo que recorda e a maneira como o recorda*". Gabriel Garcia Marquez

Professora Susana Freitas, vai ser difícil esquecer a oportunidade que me deu. Trabalhar no INESC-MN foi uma aventura da qual guardo muitas recordações e lições de vida. Obrigado.

Simon Knudde, I have you to thank for all the hours of discussion. We have grown a little bit since the first time Professor introduced us. Good Luck on the MgO single crystal target!

Anastasiia Moskaltsova and Sylvain Martin, thank you for all the tips and advices.

Ricardo Cardoso, "estou de sonho de vida". Obrigado pela tour ao INESC.

Filipe Cardoso, obrigado pela paciência e pelos conselhos. Muita sorte para a Magnomics e para ti, tu mereces.

João Valadeiro e Paulo Coelho, boa sorte com os futuros Doutoramentos e obrigado pela camaradagem durante a minha passagem pelo INESC-MN.

Fernando Franco, o programa de análise de dados de MR ficou impecável! Obrigado pelas horas de trabalho de Ctrl+C e Ctrl+V que o teu programa evitou.

Ana Silva, obrigado por me mostrares que é possível ser calmo e ter capacidade de decisão, mesmo nos momentos de maior tensão e volume de trabalho.

Obrigado aos Engenheiros de Processo do INESC-MN, Fernando Silva, José Bernardo e Virgínia Soares.

Obrigado pelos 5 anos de camaradagem, jantares, conversas amenas e "ratadas". João "Garcia" Coelho, Miguel "Mi" Teixeira, Tiago "Tássio" Santos, Hugo "Estiloso" Dias. Aos da velha guarda, Digníssimos Tiago Gomes e Ricardo Cardoso.

António Galla, Luís Albuquerque, João Sousa, José Ferraz e Pedro Viegas. Já passaram quase 7 anos desde que me "aturam" a falar sobre Materiais. Um grande abraço e vemo-nos no próximo jantar.

Ana Braga, a estabilidade é uma das chaves para o sucesso. Obrigado.

Estarei para sempre grato pela bolsa MiguelNetoIST/2009/11101991, projeto suportado financeiramente por Pai e Mãe Lda.

Resumo

A investigação apresentada neste trabalho tem como foco principal o desenvolvimento e otimização de estruturas de junções de efeito túnel. As junções de efeito túnel produzidas neste trabalho possuem barreiras de AlOx obtidas por Oxidação Natural. Verifica-se que a espessura do alumínio é um fator determinante para as propriedades das estruturas produzidas por este método. Mostra-se que é possível obter valores de TMR de 20 % com um RxA de 180 $\Omega.\mu m^2$. Foram produzidas 2 séries de amostras com electrodos diferentes, uma série com CoFeB e outra de CoFe. Estas séries são comparadas e a série de CoFeB mostra ser capaz de obter resultados melhores para as condições estudadas.

Um estudo que determina o número de camadas magnéticas mortas revela a importância do boro. Camadas magnéticas mortas na ordem dos 2 Å foram medidas para a interface de CoFe/AlOx e 6Å para a interface CoFe/AlOx. A sua variação com a temperatura também é discutida.

Um estudo da influência da camada de semente no sistema de MnIr/CoFe permitiu obter valores de polarização de intercâmbio de 310 Oe e coercividade de 19 Oe.

KEY-WORDS:

AlOx barrier; Junções de Efeito de Túnel ; Camadas Magnéticas Mortas; Polarização de Intercâmbio MnIr/CoFe; Oxidação Natural;

Abstract

The research conducted in this study is primarily focused on the development and optimization of MTJ structures. The film stack explored in this work is CoFeB/AlOx-based, where the AlOx was obtain by Natural Oxidation. A dependence of the aluminum thickness is shown and a TMR of 20% with an RxA of 180 $\Omega.\mu m^2$. A series of CoFeB and CoFe are compared. The CoFe shows a limitation for the production of thin barriers by Natural Oxidation due to its proneness to oxidation.

A Magnetic Dead Layer study was conducted revealing the importance of Boron in the CoFeB alloys. Magnetic Dead Layers of 2 Å were measured for the CoFeB/AlOx interface and 6 Å for the CoFe/AlOx interface. The influence of the annealing temperature is also discussed in the MDL thickness.

The study of the influence of the seed layer in the MnIr/CoFe exchange bias system is show reaching values of $H_e = 310\ Oe$ and $H_c = 19\ Oe$.

KEY-WORDS:

AlOx barrier; Magnetic Tunnel Junction; Magnetic Dead Layer; Exchange Bias MnIr/CoFe; Natural Oxidation;

Index

List of Figures

List of Tables

List of Abbreviations

AC	Alternating Current
AFM	Antiferromagnet
CIP	Current-in-plane
DC	Direct Current
DM	Diamagnetic
DWL	Direct Write Laser
FM	Ferromagnetic
GMR	Giant Magnetoresistance
IBD	Ion Beam Deposition
IPA	Isopropanol
MR	Magnetoresistance ratio
NM	Non-magnetic
MTJ	Magnetic Tunnel Junctions
PM	Paramagnetic
PR	Photoresist
PVD	Physical Vapor Deposition
RF	Radio Frequency
SAF	Synthetic AntiFerromagnets
TMR	Tunnel Magnetoresistance
UHV	Ultra High Vacuum
VSM	Vibrating Sample Magnetometer

1 Introduction

The discovery of novel physical phenomena at practical temperatures in ferromagnetic metal-based systems, such as spin-dependent scattering and tunneling, has resulted in rapid development of advance storage and memory devices. Storage hard drives using the giant magnetoresistance (GMR) heads started to be commercialized by IBM in 1997 and have won Stuart Parkin, its inventor, the Millennium Technology prize in 2014. Significant progress has also been made in the development of tunneling magnetoresistance (TMR)-based memory, sensor and storage devices in bringing them closer to commercialization.

INESC Microsistemas e Nanotecnologias (INESC MN) is a private, non-profit Research and Development Institute created in January 2002. INESC-MN has a strong background on thin film preparation, by magnetron sputtering and ion beam deposition. AlOx and MgO – based tunnel junctions for application in read heads, sensors and MRAM have been the focus of research of the group since its foundation.

The aim of this thesis is to continue the Research and Development efforts in understanding and optimization of MTJ stacks with Alumina barrier. State of the art results have been published previously at INESC-MN back in 1999, however the high values of TMR showed by MgO barriers have diminished significantly the interest in AlOx barriers. Lately, MgO barriers have shown limitation namely in sensing low magnetic fields due to its intrinsic noise. This fact has lead to the a higher interest in the AlOx barriers.

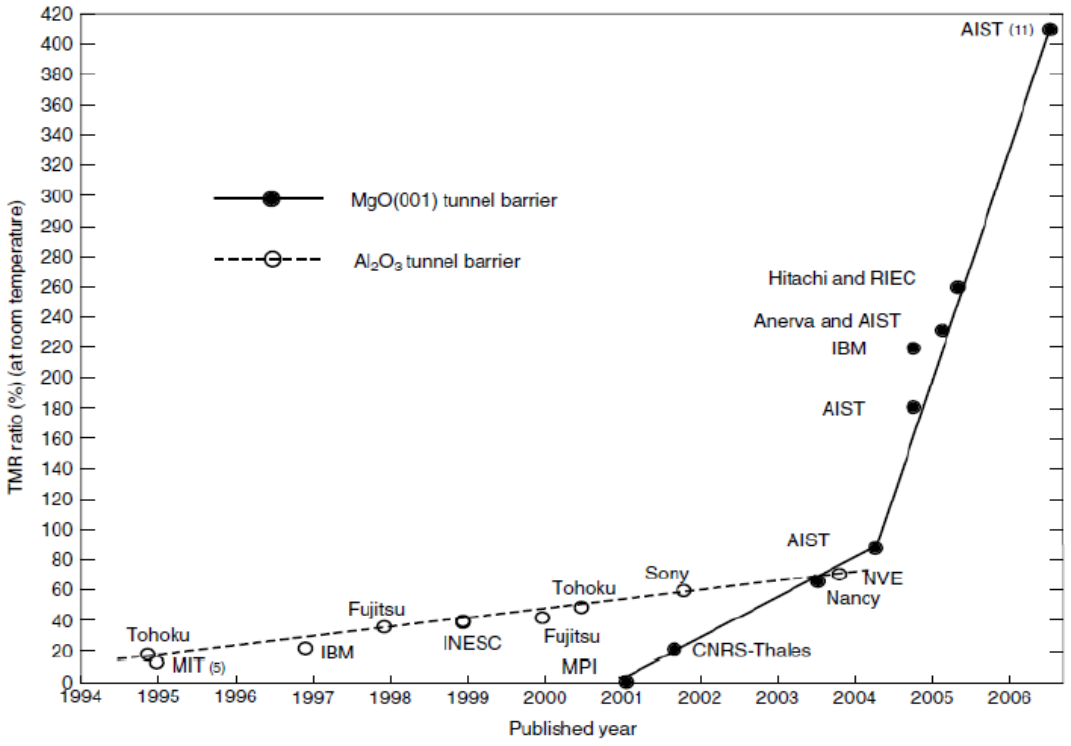

Figure 1 –The evolution of TMR ratio (%) at room temperature for the AlOx and MgO barriers since 1995 until 2006.

This thesis aims to understand the natural oxidation process and the oxygen diffusion between the AlOx barrier and the electrodes of CoFeB and CoFe. The work presented in this Master Thesis was developed in the ISO 4 and ISO 5 cleanrooms from INESC-MN.

1.1 Magnetic Thin Films Concepts

1.1.1 Exchange Bias

Exchange bias is a coupling phenomena observed in an AFM/FM interface. The phenomenon was first identified in 1956 by Meiklejohn and Bean. This phenomenon causes the hysteresis loop of the FM to be shifted to by an offset field value, identified as exchange bias (H_E). There are two possible configurations to observe the exchange bias, top and bottom configuration. In top configuration the AFM in grown on top of the FM, in bottom is the other way around. In order to observe exchange bias in bottom configuration is almost always needed cooling the AFM/FM interface in the presence of a static magnetic field from a temperature higher than a minimum, designated as **Blocking Temperature** (T_B).

Several theoretical approaches have been made to explain the exchange bias phenomena, the most important models are: phenomenological model with ideal interfaces; interfacial AFM domain wall model; random field model; spin-flop perpendicular interfacial coupling and uncompensated interfacial AFM spins. A complete review of experimental results and theoretical models can be found in [1] [2] [3].

The first model of exchange bias assumes an ideal interface between the ferromagnetic and antiferromagnetic layers. The interface is considered atomically smooth and single crystalline. The AFM materials spin structure as shown in the schematic in Figure 2 a), results in a plane of fully uncompensated spins at the FM/AFM interface. In this ideal model, the spins of the FM layer rotate coherently while the spins of the AFM layer remain fixed. The energy cost is equal to the interfacial exchange energy and the resulting exchange bias is given by

$$\boldsymbol{H_E = \frac{\Delta\sigma}{M_{FM}t_{FM}} = \frac{2J_{ex}S_{FM}S_{AFM}}{a^2M_{FM}t_{FM}}} \quad (1)$$

Where $\Delta\sigma$ is the interfacial exchange energy density, M_{FM} is the magnetization saturation of the FM, t_{FM} is the thickness of the FM layer. J_{ex} is the exchange parameter, S_{FM} and S_{AFM} are the spins of the interfacial atoms, and a is the cubic lattice parameter [1].

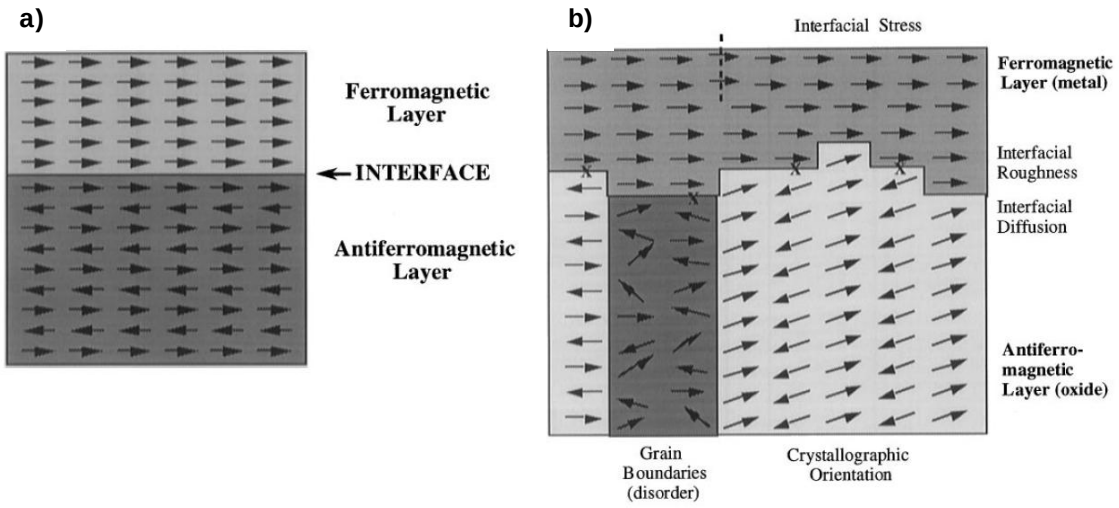

Figure 2 – a) Schematic of the ideal FM/AFM interface. The interfacial AFM spin plane is a fully uncompensated spin plane. b) Interfacial complexities of a polycrystalline FM/AFM interface. ***[1]***

The experimentally observed exchange fields are about half of the values predicted by this model [4]. This is attributed to the fact that this simple model does not represent realistically the FM/AFM interfacial environment. Phenomena such as diffusion at the interface or roughness have to be taken into consideration for the reduction of the exchange bias. **Error! Reference source not ound.** b) schematically shows the interfacial complexity of a polycrystalline FM/AFM interface. Roughness, in the form of the interfacial atomic steps could produce neighboring antiparallel spins, thereby reduce the number interfacial uncompensated spins.

For thin films the magnitude of H_E is closely linked to the crystalline structure of the **seed layer**, the layer where the AFM thin film growth is promoted, as shown by the study presented in 3.2.1 and 3.2.2.

1.2 Magnetic Tunnel Junction Concepts

1.2.1 Tunnel Magnetoresistance (TMR) effect

A Magnetic Tunnel Junction (MTJ) stack is a thin film stack of two ferromagnetic layers separated by a thin insulator layer (5 – 30 Å), e.g. AlO_x. In these devices one ferromagnetic layer has its magnetization pinned while the other is allowed to move freely under the influence of external magnetic fields. There are two possible configurations depending on the relative position of the pinned layer to the barrier.

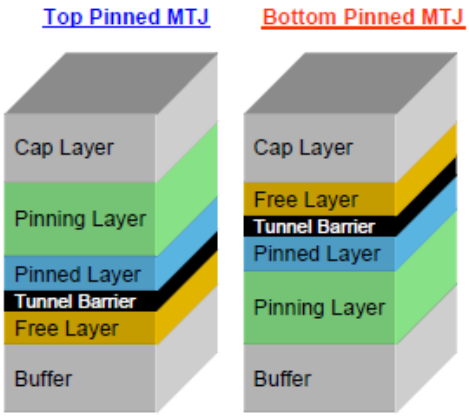

Figure 3 – Schematic stack structure of a MTJ. Two structures depending on the FM layer which is used as reference.

The resistance is lowest when the magnetizations of the ferromagnetic layers are parallel (R_{min}), while antiparallel the resistance is high (R_{max}). This change in resistance with the relative orientation of the two magnetic layers, called Magnetoresistance Ratio effect, is one of the most important phenomena in spintronics. The size of this effect is measured by the magnetoresistance ratio (MR):

$$MR = \frac{R_{max} - R_{min}}{R_{min}} \tag{2}$$

Julliere observed this effect for the first time in 1975 at 4.2 K [5] and it was only in 1995 that Moodera et al [6] were able to produce Magnetic Tunnel Junction with amorphous aluminum oxide tunnel barriers with MR ratios as high as 18% at Room Temperature. Room-temperature MR ratios have been increased to about 70% [7] by optimizing the ferromagnetic materials and the conditions for fabricating the Al-O barrier.

In 2001 first-principle calculations predicted that epitaxial MTJs with a crystalline magnesium oxide (MgO) tunnel barrier would have MR ratios of over 1000% and in 2004 MR ratios of about 200% were obtained at RT in MTJs with a crystalline MgO (001) barrier. The high increase in MR value from Alumina to MgO barriers is due to the crystalline nature of the MgO barrier. In MTJ comprising an amorphous barrier, the TMR only originates from the difference in densities of states at the Fermi level for spin up and down electrons along the interface between the tunnel barrier and the adjacent magnetic layer. In MTJ comprising a crystalline barrier, another phenomenon takes place: there is a filtering of the tunneling electron according to the symmetry of their wave function. [8]

The tunneling MR can be understood in terms of a two-band model in which the d-band is split into spin-up and spin-down bands with different density of states at the Fermi energy. When the magnetization of the layers is parallel, the majority-band electrons tunnel across to the majority band of the opposing ferromagnetic layer and the minority to the minority band. When they are antiparallel, the majority/minority band electrons are forced to tunnel into the minority/majority band of the opposing

ferromagnetic. The reduced number of states available for tunneling between the ferromagnetic layers when the layers are antiparallel results in an increased tunneling resistance, as compared to parallel.

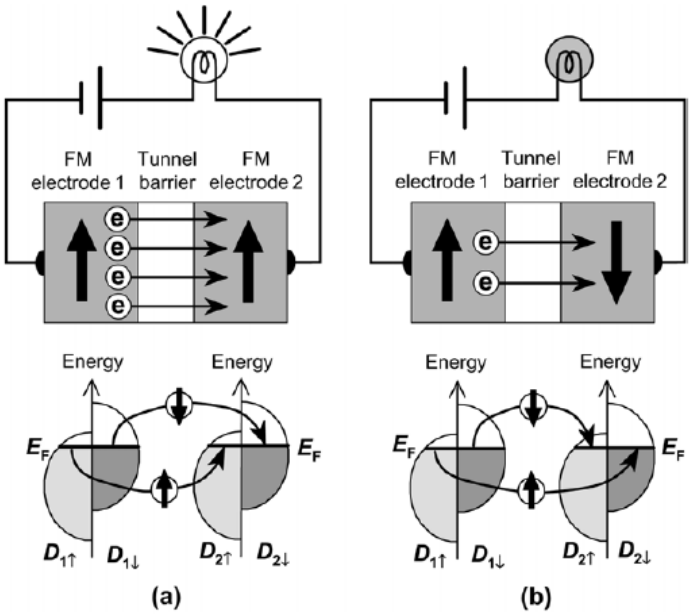

Figure 4 – Systematic ilustration of TMR effect in a MTJ: a) Magnetization in the two electrodes are align parallel (P state). B) Magnetization are aligned antiparallel (AP state). $\boldsymbol{D_1}$ refers to the density of states at Fermi Energy for the majority-spin and minority-spin bands in electrode 1. $\boldsymbol{D_2}$ refers to the density of states at Fermi Energy for the majority-spin and minority-spin bands in electrode 2. Adapted from ***[9]***

When applying a bias voltage between these electrodes, current flows through the stack, perpendicularly to the interfaces causing the electrons to tunnel through the insulating tunneling barrier. The electrons emitted from one ferromagnetic layer are spin-polarized in a direction parallel to the magnetization of the emitting electrode. Their probability of going through the barrier depends on the magnetic state of the receiving electrode. As a result, the resistance of the stack depends on the relative orientation of the magnetization in the two ferromagnetic layers adjacent to the barrier.

1.2.2 Resistance of a MTJ stack

In MTJ, the resistance of the stack is largely dominated by the resistance of the tunneling barrier itself. The latter varies exponentially with its thickness, The right quantity for characterizing the resistance of the barrier is its Resistance Area product most often written as RxA product and can range from tenth of $\Omega.\mu m^2$ up to $M\Omega.\mu m^2$. [8]

2 Process Equipment and experimental techniques

2.1 Thin Film Deposition

The thin film deposition presented on this work was produced by a Nordiko 3600 machine, in an ISO 5 Class Clean Room at INESC-MN. The substrates used were 2.5x2.5 cm glass previously cleaned in an Alconox solution. The method used for thin film deposition was Ion Beam Deposition, with Xe ion beam. The deposited samples were deposited, processed and characterized between February and August 2014.

2.1.1 Nordiko 3600 overview

The Nordiko 3600 Ion Beam tool was installed at INESC-MN during 2005 and is able to process 8 inch wafers. Besides thin film deposition, the Nordiko 3600 was used as Ion Milling tool for the presented work.

The Nordiko 3600 Ion Beam System is divided in 3 modules: the Chamber (1), the Dealer (2) and the LoadLock (3), which are separated by a system of guillotine gate valve. The Figure 5 illustrates the machine in cross section and the mechanism of the wafer transport.

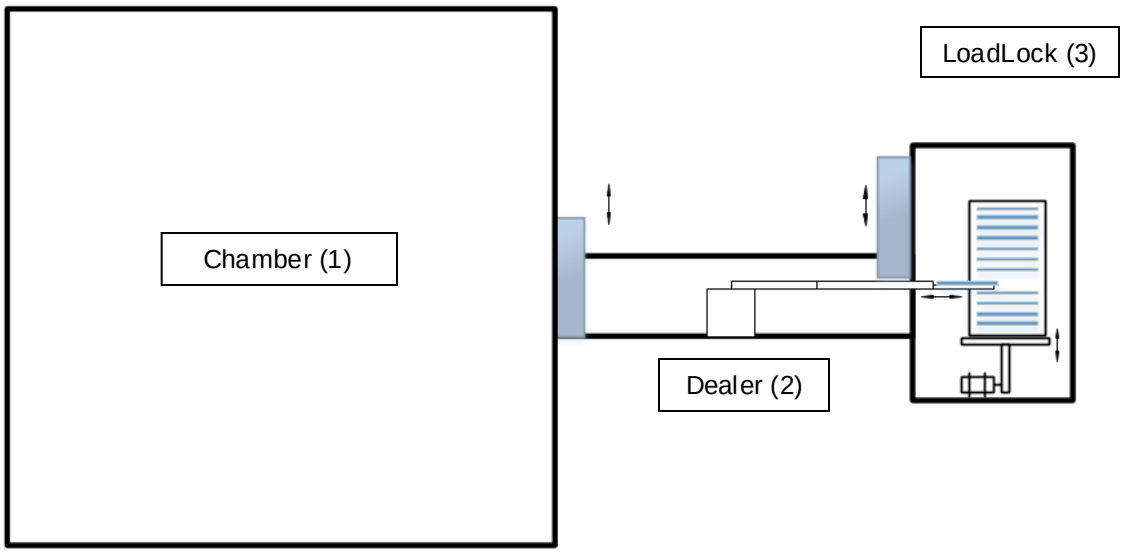

Figure 5 - Schematic of Nordiko 3600 cross-section and loading/unloading mechanism.

The wafers are placed by the user in the Cassette (3.1), until a maximum number of 12. The pressure in the Load Lock (3) is deceased until 10^{-7} Torr in two steps; first a mechanical rough pump is activated followed by opening the cryogenic pump valve. The pressure reaches the desired value in roughly 3 minutes. When the pressure is reached the gate valve that separates the LoadLock (3) from the Dealer (2) is opened and the robotic arm picks and transfers the desired wafer into the Chamber (1).

In Nordiko 3600 system the wafers are loaded one by one. In order for it to pick different wafers, the Cassette (3.1) is equipped with a lift under it so that depending on its height the arm picks the wafer for the desired process parameters.

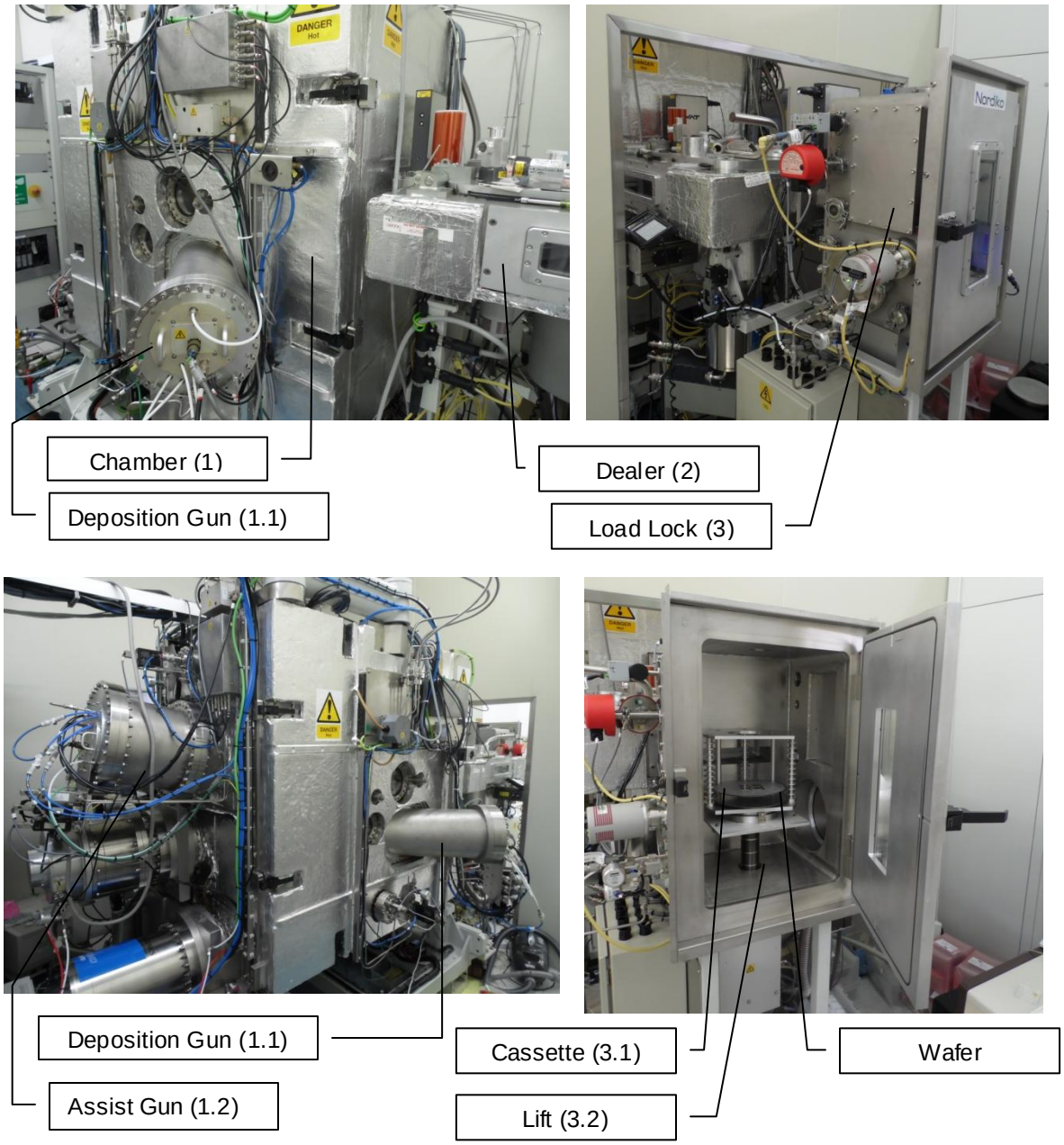

Figure 6 - Photographs of the N3600 at INESC-MN (*taken at 19 of August 2014*). a) Chamber, Dealer and Deposition Gun. b) Chamber showing the Assist Gun and the Cryogenic Pump. c) Load Lock and Dealer. d) Open Load Lock showing the placement of wafer on the Cassette.

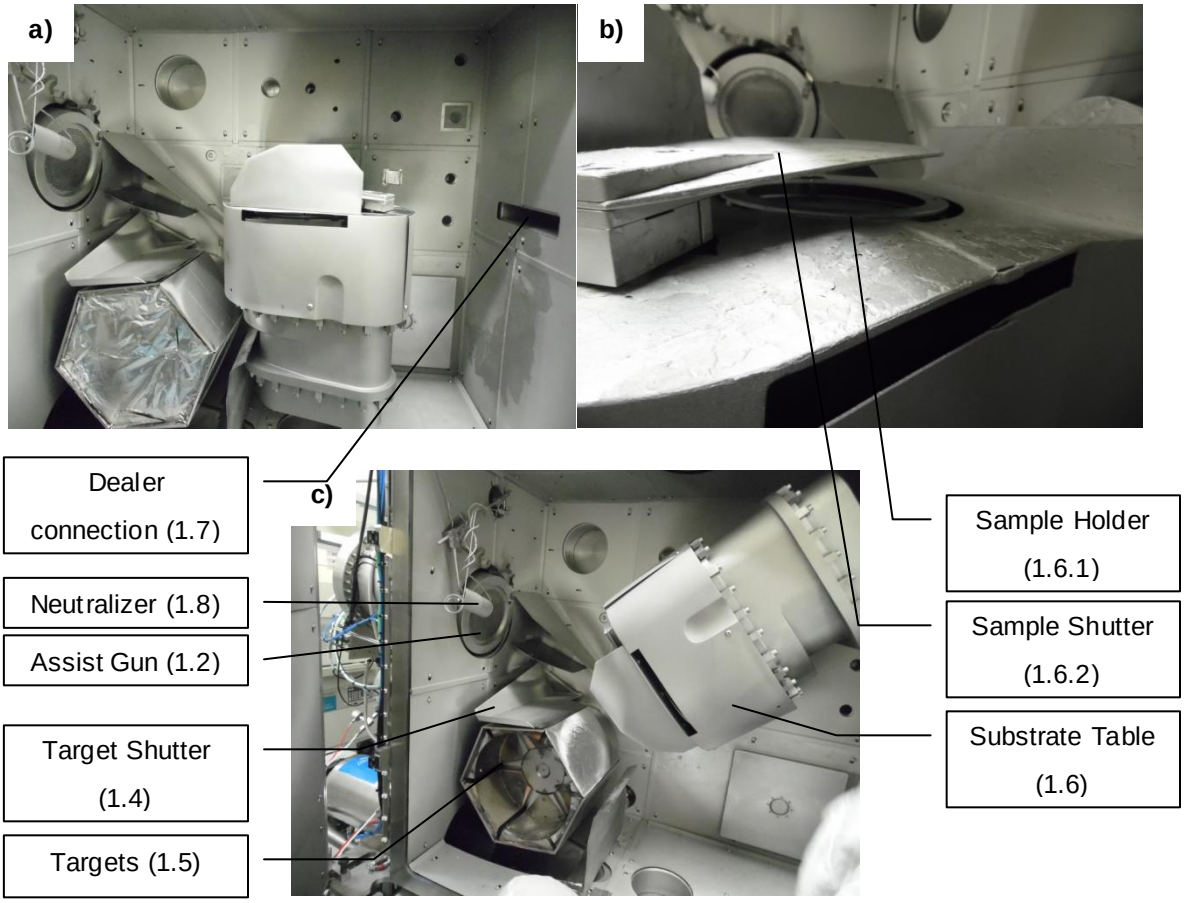

Figure 7 - Photograph of the inside of the N3600 Chamber at INESC-MN (*taken at 11 of August 2014*). a) Substrate table at 0 deg.b) Substrate table and shutter. c) Substrate table at 130 deg.

The system incorporates two ion beam guns (Deposition Gun (1.1) and Assist Gun (1.2)), a Substrate Table (1.6) and a Target Assembly (1.5). The Target Assembly (1.5), comprising 6 targets, can rotate around its axis in order to align each target with the direction of the beam. The Target Shutter (1.4) protects the target in order to minimize the target contamination during process, either deposition of other materials or Ion Milling processes.

The samples are loaded from the Cassette (3.1) through the Dealer gate (1.7) and placed on the Substrate Holder (1.6.1). On the Substrate Table (1.6) an electromagnet is used to produce a uniform and constant 50 Oe magnetic field over the wafer. The purpose of this field is to break the anisotropy, defining easy axis and hard axis directions during the deposition of magnetic materials. The Sample Shutter (1.6.2) covers the Substrate Table (1.6) protecting the samples during the guns preparation steps. In timed processes, the opening of the Sample Shutter (1.6.2) coincides with the beginning of the countdown. The Substrate Holder (1.6.2) rotation can be controlled and is set to 30 rpm, improving the substrate uniformity not only on the Deposition but also in the Ion Milling processes. Furthermore, the Substrate Table (1.6) can be tilted in order to change the angle between the substrate and the Ion Beams and perform the loading and unloading steps. At 0 deg angle means that the table is horizontal, which corresponds to the

loading/unloading of the wafer (Figure 7 a), while a 130 or 180 pan angle are common angles used to perform assisted and non-assisted deposition (Figure 7 c), respectively. For Ion Milling, where only the assisted gun (1.3) is used, 30 and 60 deg are commonly used.

Pointed at the ion beams originated from the Assist Gun (1.3) and Deposition Gun (1.1), two Neutralizers (1.8) emit electrons with the purpose of neutralizing the ion beam. This is an especially important step in order to deposit Insulating targets, since it avoids a charge accumulation over the surface of the target.

2.1.1.1 Nordiko 3600 User Interface

In order to automatically run a process, the parameters and their sequence must be defined. So in the Nordiko 3600 software the functions are grouped in hierarchical structures which are created by the operator:

- The most basic block are the ***process steps***, where the parameters used in the ion beam guns and neutralizers, the substrate table pan angle and rotation, and the time which the process should last.
- Sequences of process steps are grouped in ***wafer recipes***. The wafer recipe always starts with a *Load Wafer* process step and finishes with an *End Function*.
- Finally, wafer recipes are associated with specific wafers in a ***batch***. During a batch a wafer can be loaded any number of times to perform any wafer recipe.

Once the wafer is loaded the parameters for the first process step are loaded and the deposition is started.

2.1.1.2 Ion Beam Deposition

Ion Beam deposition is a process that uses an ion beam to sputter a material onto a substrate. In Nordiko 3600 a Xe plasma is created, accelerated against the target and consequently deflected to the substrate. This is commonly indentified as a secondary ion beam deposition or ion sputter deposition [10].

The plasma is created in the vacuum chamber of the Deposition Gun. The power required to ionize the gas atoms is provided through a Radio Frequency antenna exited by a 13.56 Mhz RF power supply. A set of three voltage biased grids is used to accelerate the plasma ions and focus the beam against the target.

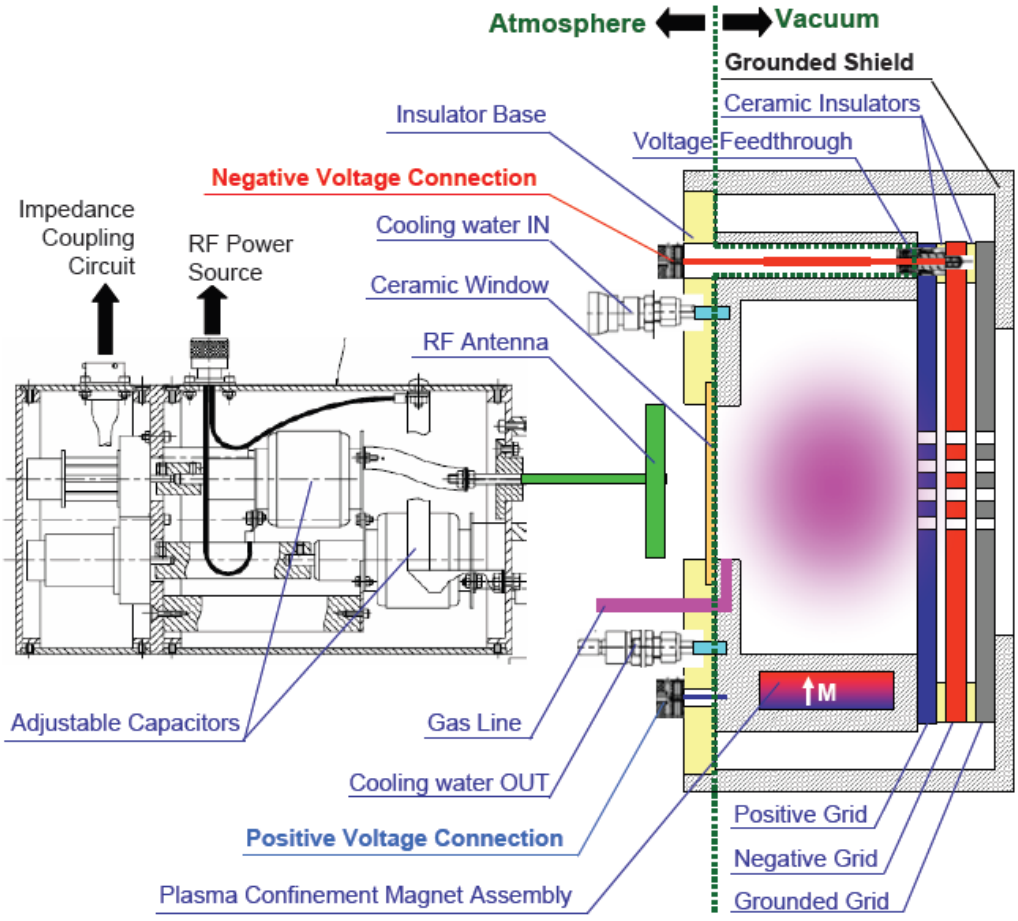

Figure 8 – Schematic view of N3000 Deposition Gun ***[11]***.

The strike sequence starts with the pressure build up in the gas line, followed by applying RF Power. Next the Mass flow controller adjusts the gas flux so that the Reflected Power reaches the value 0, meaning the Xe ions formed a stable plasma. Finally, voltages are applied to the grids and consequently the plasma ions are extracted and accelerated. Both the positive and negative grids are connected to sources supplying positive and negative voltage bias. The outer ground is in direct contact with the gun shield which is connected to the grounded chamber wall.

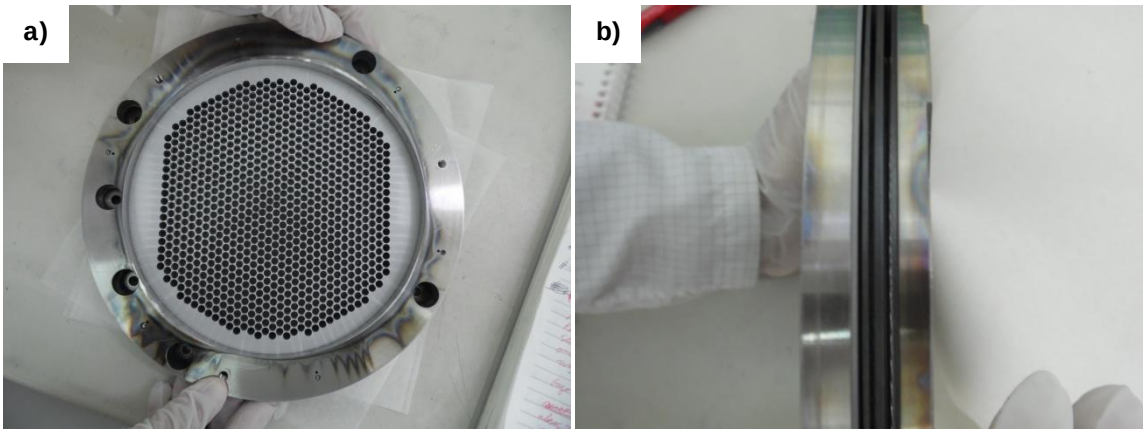

Figure 9 – Photographs of the grid set used in the Deposition Gun of Nordiko 3600 machine. a) top view; b) side view.

The plasma Ions accelerated by the grids towards the target carries with it a kinetic energy which are transferred to the target atoms thus sputtered and deposited over the sample substrate. The deposition rate of the target atoms is related with the geometry of the system (angle between the target surface and the ion beam, distance between the target and the ion gun, beam profile, relative angles of target surface and sample surface and distance between target and sample) but also of the energy carried by the ion beam.

Table 1 – Deposition Gun conditions for Deposition process.

Deposition Gun	*RF Power*	*V1(+)*	*I+*	*V2(-)*	*V3(-)*	*Xe Flow*	*Pressure*
Setpoint Reading	150-200W	1200V	+171 mA	-275V	50V	4 sccm	1×10^{-4} Torr

Substrate Table	*Rotation*	*Angle*	*Field*
Setpoint Reading	30 rpm	181 deg	50 Oe

The targets used for this work were: NiFeCr, Ru, Al, CoFe, CoFeB and MnIr. In the first section of the experimental work Ta was used but was replaced by NiFeCr, as further explained in 3.2.1. The CoFe and CoFeB composition were determined by Rutherford Backscattering technique in 20 March 2014, further details can be found in 3.1.1.

The deposition rates (see Table 2) in this work were obtained by depositing during a specific time and measuring its thickness a profilometer.

Table 2 - Target and Deposition rate.

Target's material	Deposition Rate (Å/s)
Ta	0.60
Ru	0.71
MnIr	0.70
Al	1.08
NiFeCr	1
CoFe	0.97
CoFeB	0.51

2.1.1.3 Ion Milling

The Assist Gun is similar to the Deposition Gun, but instead this provides a direct and uniform beam over the substrate samples. This allows the system to process wafers in Ion Milling, assisted deposition and ion beam smoothing processes. During this work the assist gun was only used to perform Ion Milling.

The standard conditions to Ion Milling are presented in Table 3. The 60 and 30 degree conditions were used for different purposes. The 60 degree was used to minimize shadow effects, while the

30 degree was used in step of the MTJ pillar definition in order to minimize re-deposition of the milled material on the lateral faces of the pillar.

Table 3 – Assist Gun conditions for Ion Milling Process

Assist Gun	*RF Power*	*V+*	*I+*	*V-*	*Ar Flow*	*Pressure*
Setpoint Reading	150-200W	735V	+105 mA	-350V	10 sccm	1 x 10^{-4} Torr

Substrate Table	*Rotation*	*Angle*
Setpoint Reading	30 rpm	30/60 deg

2.1.2 UHV II

UHV II is a machine used for oxide deposition by sputtering from a 6 inch diameter 99.995% Al_2O_3 target. The UHV II is located in a ISO 5 clean room. This system was used for the depositing a 1000 Å insulating layer in order to insure that the electrons only flow through the MTJs pillar.

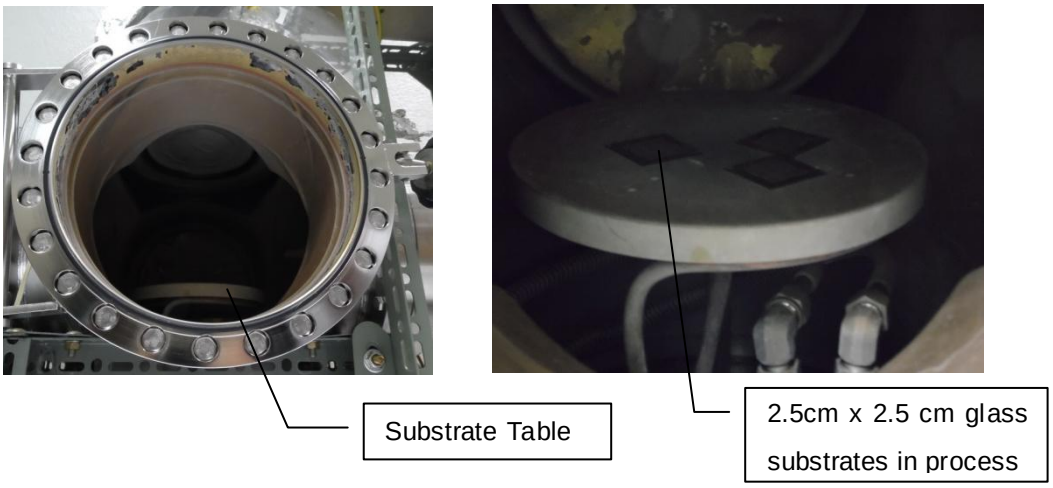

Figure 10 – Photographs from the inside chamber of UHV II machine.

This machine has inside the chamber only one target facing down and allows deposition of samples of 6 inch in diameter. Pressures of 3x10^{-7} Torr are needed to obtain the optimum deposition conditions. The deposition conditions are as follow:

Table 4 – Al_2O_3 Deposition conditions in UHV II.

UHV II	*RF Power*	*Pressure*	*Gas Flow*	*Deposition Rate*
Al_2O_3 Deposition	200W	2.0 mTorr	4 sccm	~ 11 A/min

2.1.3 Nordiko 7000

Nordiko 7000, installed in an ISO 4 clean room, is an automated cluster system, composed by a Load Lock connected to four chambers through a distribution chamber (dealer). This system was designed to operate with 6 inch diameter wafers. However one square inch can be processed using adapted 6 inch diameter holders.

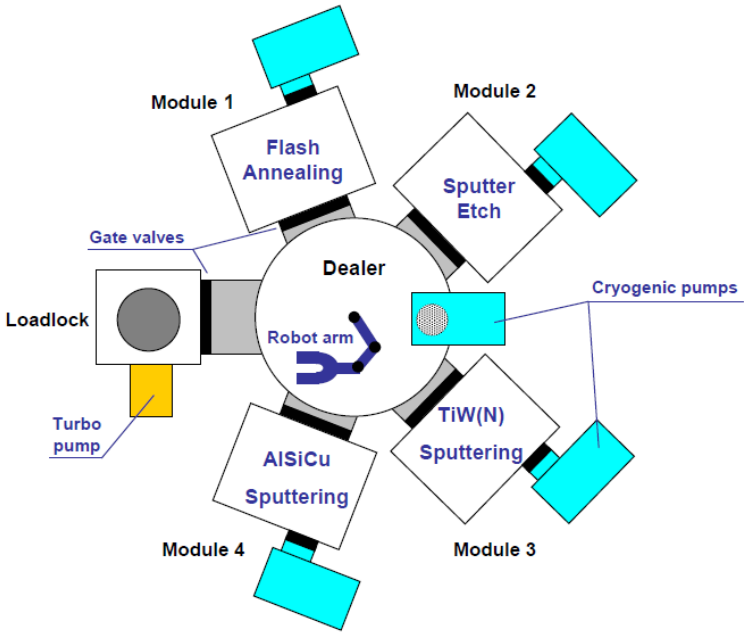

Figure 11 – N7000 schematic drawing ***[11]***

This system was used for the deposition of Al 3000 Å/TiW(N) 150 Å layers in the Top Contact Deposition Step. The films are deposited by sputtering (using Ar ions) from a sintered $Ti_{10}W_{90}$ target. During the deposition a flow of N_2 is used so that the deposited films incorporate ~50% of nitrogen which improves the passivation properties of the TiW layer. The process conditions are as follows:

Table 5 – Process conditions used in each Module of the Nordiko 7000 to deposit the Top Contact.

Module 2	*Ar Flow*	*RF Bias*	*RF Power*	*Pressure*	*Time*
Sputter Etch	50 sccm	40 W	60 W	3 mTorr	60 s

Module 3	*Ar Flow*	*N flow*	*DC Power*	*Pressure*	*Time*
TiW (N) Sputter	50 sccm	10 sccm	0.5 kW	3 mTorr	34 s

Module 4	*Ar Flow*	*DC Power*	*Separation*	*Pressure*	*Time*
AlSiCu Sputter	50 sccm	2 kW	82 %	3 mTorr	80 s

2.2 Magnetic measurements – VSM

SQUIDS and force-based techniques (e.g. AGM), allow measurements with RMS noise levels on the 10^{-8} emu level. SQUIDS require liquid helium even for ambient or high temperature operation, and the data acquisition process in inherently expensive and slow.

Force-based techniques, although fast, are generally limited to small samples (typically less that 2 to 3 mm). These methodologies are generally characterized by relatively poor reproducibility. Both techniques lack robustness and ease-of-use that are often desirable attributes for routine, high throughput magnetic measurement applications.

The Vibrating Sample Magnetometer (VSM) generates a graph of Magnetic Moment as a function of the Magnetic Field applied. A sequence of pre-defined values for the Magnetic Field is defined by the user depending on the sample and type of study.

The sample is placed into a silica glass rod which centers the sample between two pole pieces of an electromagnet that generates a homogeneous magnetic field. The distance between the two pick up coils is 1.8 cm.

The VSM working principle is based on Faraday's law which states that and electromagnetic force is generated in a coil when there is a change in flux linking the pickup coils. The oscillating magnetic field of the vibrating sample induces a voltage in the stationary detection coils, and from measurements of this voltage the magnetic properties of the sample are deduced.

In the measurement setup, the magnetic sample vibrates with a given frequency and amplitude between the two pickup coils. The silica glass rod is connected to a piezoelectric crystal, which makes the sample vibrate during the experiment.

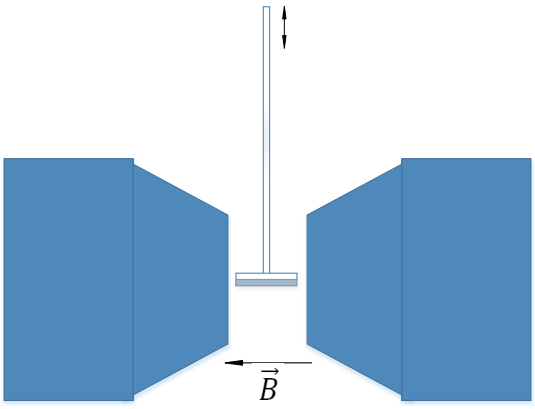

Figure 12 – Schematic of the VSM measurement setup.

For the measurements a calibration file was created where the diamagnetic contribution of the silica rod was measured. This was then removed to obtain the curves presented in the thesis. A commercial DMS (Digital Measurement System) model 880 vibrating sample magnetometer with field resolutions of 0.1 Oe and sensitivity of 10^{-5} emu/cm^3 was used. The set of electromagnetic coils allow a field range of 13 kOe.

2.3 Device Fabrication

Microfabrication is the process by which individual devices with dimensions in the μm range are manufactured. The detailed step-by step process can be found in the Appendix A – Runsheet, while in this subchapter only the major steps will be described in detail. In order to microfabricate MTJs the ability to selectively deposit or selectively remove material from a substrate is a requirement, thus etching, lift-off techniques and optical lithography were used.

Etching is a technique used to remove material from a substrate. This can be achieved with three major techniques: Reactive Ion Etching, Chemical Etching and Physical Etching. The technique used was Physical Etching, particularly Ion Milling. The process starts with a substrate covered with a mask that protects interest areas. In this technique all the material exposed to the beam is removed. However the areas not protected by photoresist will be removed while the protected areas will show a patterned material covering the area previously occupied by the mask, as shown in Figure 13.

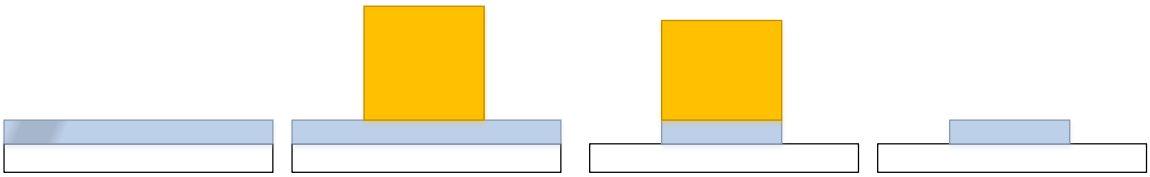

Figure 13 – Schematic of the etching microfabrication process.

On the other hand in a ***lift-off*** technique, the aim is to deposit material in areas of interest. It also starts with a substrate covered with a mask that covers a portion of it. The material that is to be patterned is then deposited over the mask. Finally the mask is removed taking with it the material covering the area previously un-occupied by the mask, as shown in Figure 14. The thickness ratio between photoresist and the deposited material used is 15:1.

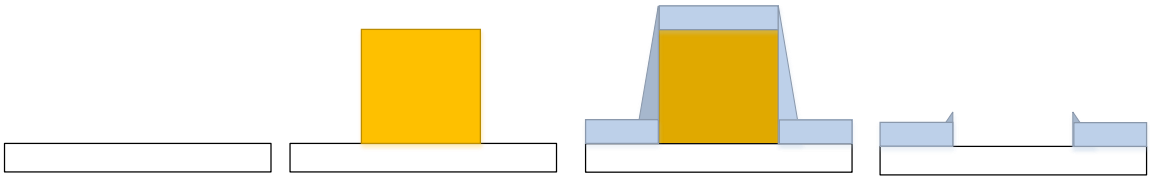

Figure 14 – Schematic of the Lift-off Microfabrication process.

The major advantage of the etching technique is that it allows the definition of very sharp features. However high control of the thickness is needed and higher thicknesses need a high process time. Thus it is used to etch small thicknesses and define sharp features.

The lift-off process is very good when used to pattern over existing material, but is not suitable to pattern multilayer. Besides that the features are often rough looking and thus not suitable to define sharp profiles.

Optical Lithography is a process used to create the micrometric patterns over the substrate using a photo sensitive polymer called photoresist.

Step 1 - Vapor Priming

The aim of this step is to improve the adhesion between the substrate and the photoresist film. This was achieved by coating the substrate with a monolayer of HDMS (hexamethyldisilazane). Vapor priming has a total duration of 30 minutes and is constituted by several steps in order to remove water residues from the surface and depositing the HDMS.

Step 2 - Coating

The aim is to create a uniform photoresist coating with 1.5 µm thickness over the glass substrate. The process is performed in the SVG coater track and it starts by dispensing a determined photoresist volume. Next the substrate is spun at 2500 rpm for 30 seconds in order to uniformly distribute the photoresist over the wafer. Next takes part a baking step at 90 °C for 60 seconds in order to evaporate the solvent and relive stresses accumulated during the spinning step.

Step 3 - Laser exposure

The substrate table has xzy freedom. The first step is to focus the laser fixing the z axis, then the origin point is determined. The next step is to load the mask and expose the areas that are meant to be developed. The diode laser used emitted a wavelength close to 440 nm. The minimum feature is close to 1 µm.

Step 4 - Resist Development

The last step of the lithography process is development. The substrate is baked at 110 ºC for 60 s, followed by a cooldown step of 30 s. Finally, a developer is used for 60 s in order to remove the exposed photoresist.

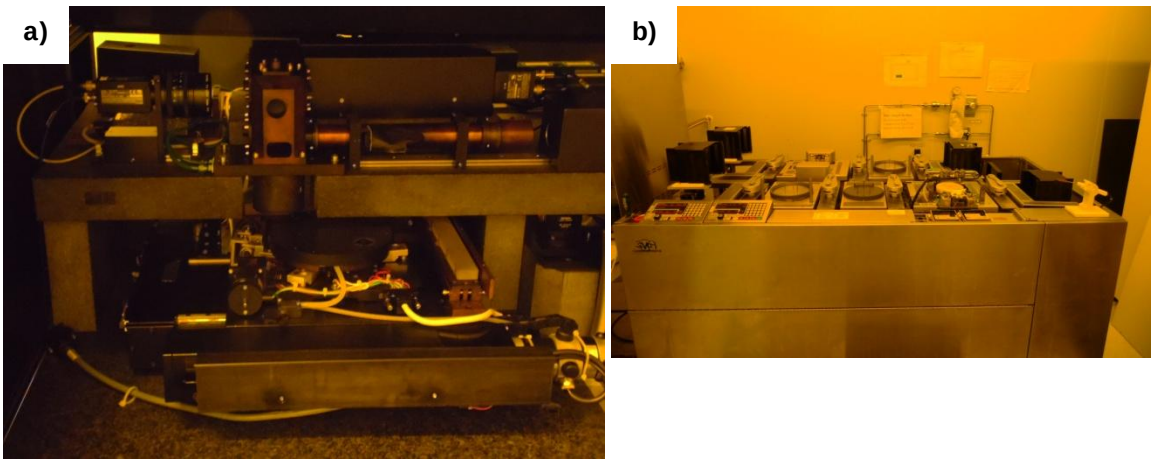

Figure 15 – Photographs taken in the yellow room: a) DWL stage and laser system; b) coating and development tracks on the SVG track system.

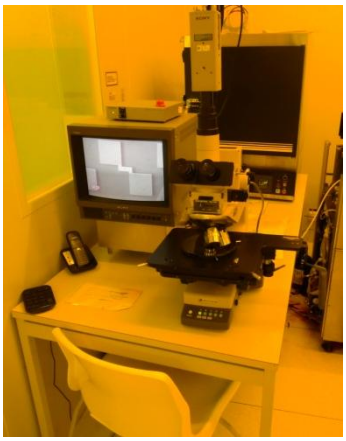

Figure 16 – Photographs taken in the yellow room of the Microscope Optical system (a bottom electrode defined by photoresist can be seen in the screen).

2.3.1 MTJ Deposition

The device fabrication process starts with the deposition of the MTJ in the Nordiko 3600 Ion Beam system, the stacks are shown in 5.2. Previously cleaned in Alconox solution 2.5cmx2.5cm glass substrates were used.

2.3.2 Bottom electrode Definition

The following step is to define the bottom electrode shape, this is accomplished by etching. Starting from the substrate with stack deposited on top of it, a photo-resist mask with the shape intended for the MTJ bottom contacted is defined using SVG tracks and the DWL. The unprotected material in the sample is then completely removed by Ion Milling in Nordiko 3600. Once the etch is completed the remaining photo-resist in the sample is removed in a resistrip process where the sample is heated up to 65 º in a solvent called *Microstrip 3001* and subjected to ultra-sounds. The sample is then subjected to an optical inspection (, where its confirm the absence of resist residues in the sample.

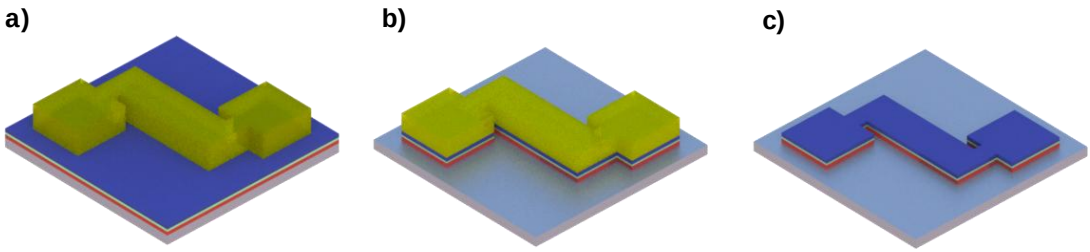

Figure 17 – Schematic of the Bottom Electrode Definition includes: a) Coating, Lithography and Development steps; b) etching process; c) Resist Strip.

2.3.3 Junction Pillar Definition

The third step is the junction pillar definition, also accomplished by etching. In the mask used only square pillars are used with a edge range of 2 to 30 μm. A two angle etch is used in order to reduce the probability of lateral MTJ deposition.

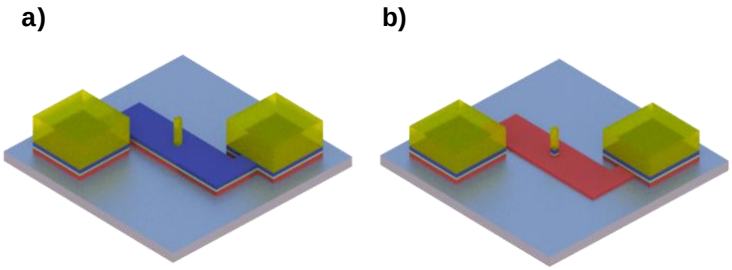

Figure 18 – Schematic of the Junction Pillar Definition includes: a) Coating, Lithography and Development steps; b) Etching process

2.3.4 Electrode Insulation

The next step is used to insulate the bottom electrode from the top electrode in such a way that the current will be lead to pass through the oxide barrier of the MTJ stack instead of directly from the bottom to the top contact. In order to do that a 1000 Å barrier of Al_2O_3 is deposited in a Ultra High Vaccum machine (UHV II) on top of the photoresist still coating areas of the substrate after the junction pillar definition step. Due to the high thickness of this oxide when compared to the oxide present in the pillar, the current will follow the easiest path and thus allowing us to measure the tunneling effect.

After the deposition of the oxide follows the lift off process, a very high time consuming step that is intended to remove the photo resist and oxide that was deposited on top of the pillar, called via opening. The time duration of this step is directly proportional to the deposited oxide thickness and inversely proportional to the pillar size.

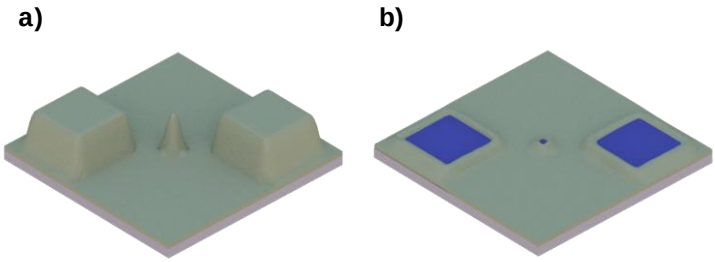

Figure 19 – Schematic of the Electrode Insulation step including: a) Oxide deposition; b) Oxide Lift-off.

2.3.5 Top Electrode Contact

The last step is the definition of the top contact. First, a lithography process is performed allowing us to define the size and shape of the top electrode, as in the previous lithography this was also preformed with the DWL and the SVG coating/developing track. Next a metallization step is preformed in the Nordiko 7000, where a layer of 3000 A of AlSiCu + a 150 A of TiW(N) is deposited over the mask, and it will over oxide, photoresist or the top electrode of the MTJ stack. The final step is the lift-off that will remove all the metal that was deposited over the photoresist.

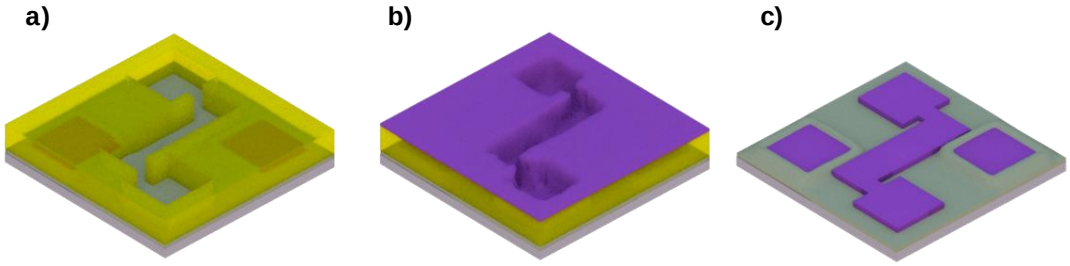

Figure 20 – Schematic of the Top Electrode Contac definition step including: a) Coating, Lithography and Development steps; b) Top Contact deposition; c) Metallic Lift-Off.

2.4 Magnetic Thermal Annealing

Magnetic thermal annealing was performed in the setup shown in Figure 21, not only for the patterned samples but also for the VSM samples with bulk stacks,

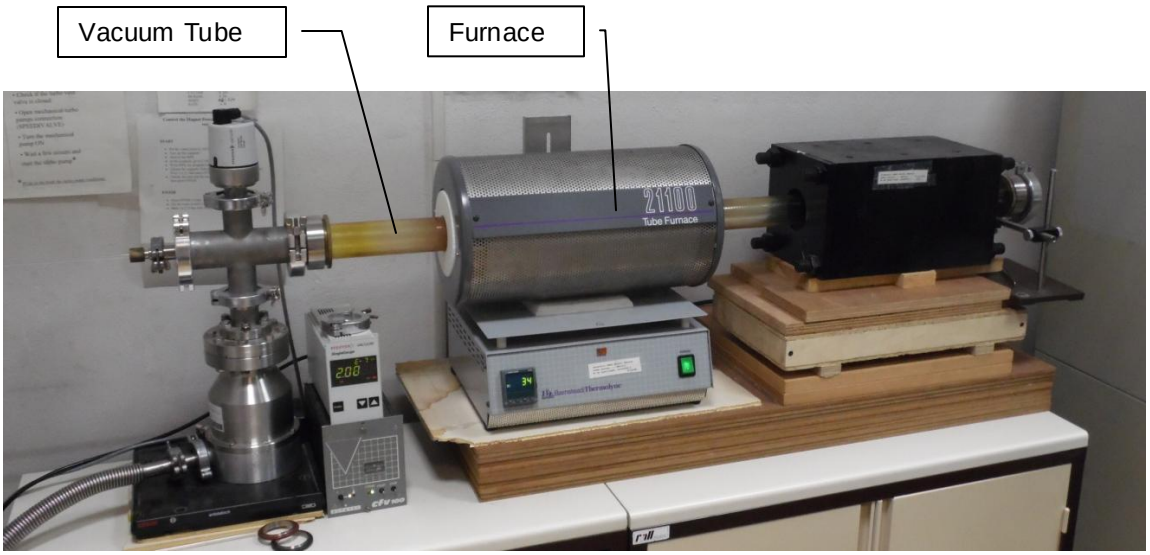

Figure 21 – Magnetic thermal annealing setup in Characterization Room at INESC-MN.

The system can be divided two parts, the furnace and a permanent magnet. In the middle of the both passes a tube, where a pressure of 1 $x10^{-7}$ can be reached using a turbo pump. The annealing process starts by placing the samples over the copper holder in such a way that the easy axis of the sample should match the permanent magnets direction. Next the copper holder is pulled inside the furnace and the vacuum tube should be closed. After the pressure reached the value of $1x10^{-6}$ the furnace can be started. In this setup the heating rate and the time at maximum temperature can be chosen. When the time ends, the furnace will stop heating so the silica rod must be manually pushed in order move the holder and the samples into the magnetic field created by the permanent magnet ($\vec{B} = 10\ 000\ Oe$), where they will cool. The furnace takes several hours cooldown, however the samples will experience a higher cool rate because they are no longer inside the furnace. Only after the 50 to 60 °C of the furnace is reached the vacuum can be broken and the samples removed.

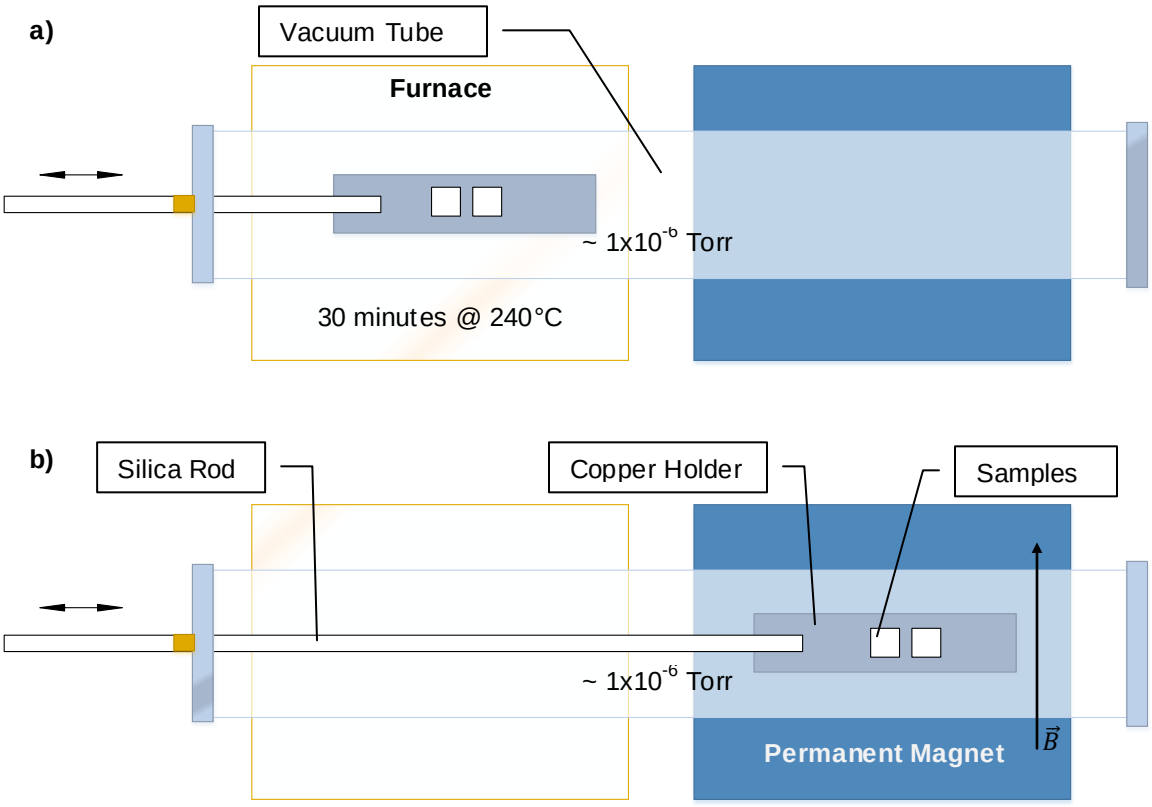

Figure 22 – Schematic of the Annealing Setup. a) Part I: Heating step, where the samples are inside the furnace; b) Part II: Cooling Step; where the sample are cooled to room temperature in Magnetic Field.

2.5 Current in Plane measurements – MR transfer curves

A measurement of the resistance as a function of the applied magnetic field as shown in Figure 23 is known as a transfer curve. Since the resistance of an MTJ depends on the relative orientation of the pinned and free layer, the transfer curve provides direct information about the magnetic configuration of a MTJ pillar.

The transfer curve measured for a particular device translates the magnetic configuration which minimizes the energy at each field point. For this work only square pillars shapes were measured, a mask with pillars from 2 μm to 30 μm was design as is presented in Appendix B – Mask.

The TMR extracted from the transfer curve is related to the spin polarization at the barrier/ferromagnetic interfaces.

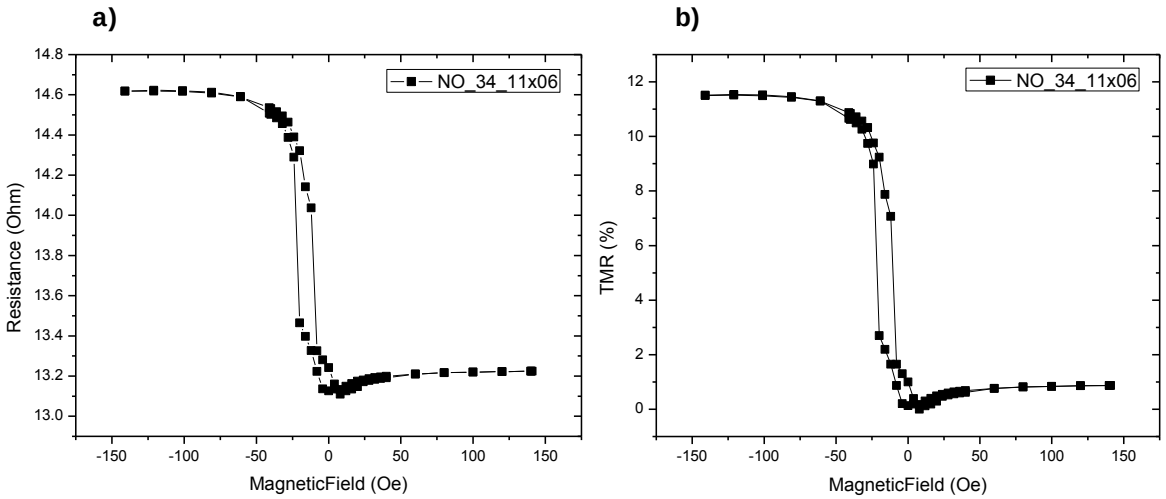

Figure 23 – 6 μm pillar from NO_34 annealed 30 min at 240 °C. a) RvsH; b) TMRvsH

The measurement of the MR transfer curves were performed in the characterization room of INESC-MN. The MR curves were obtained from patterned samples. The coils of the setup are controlled by current and have a maximum magnetic field of 140 Oe.

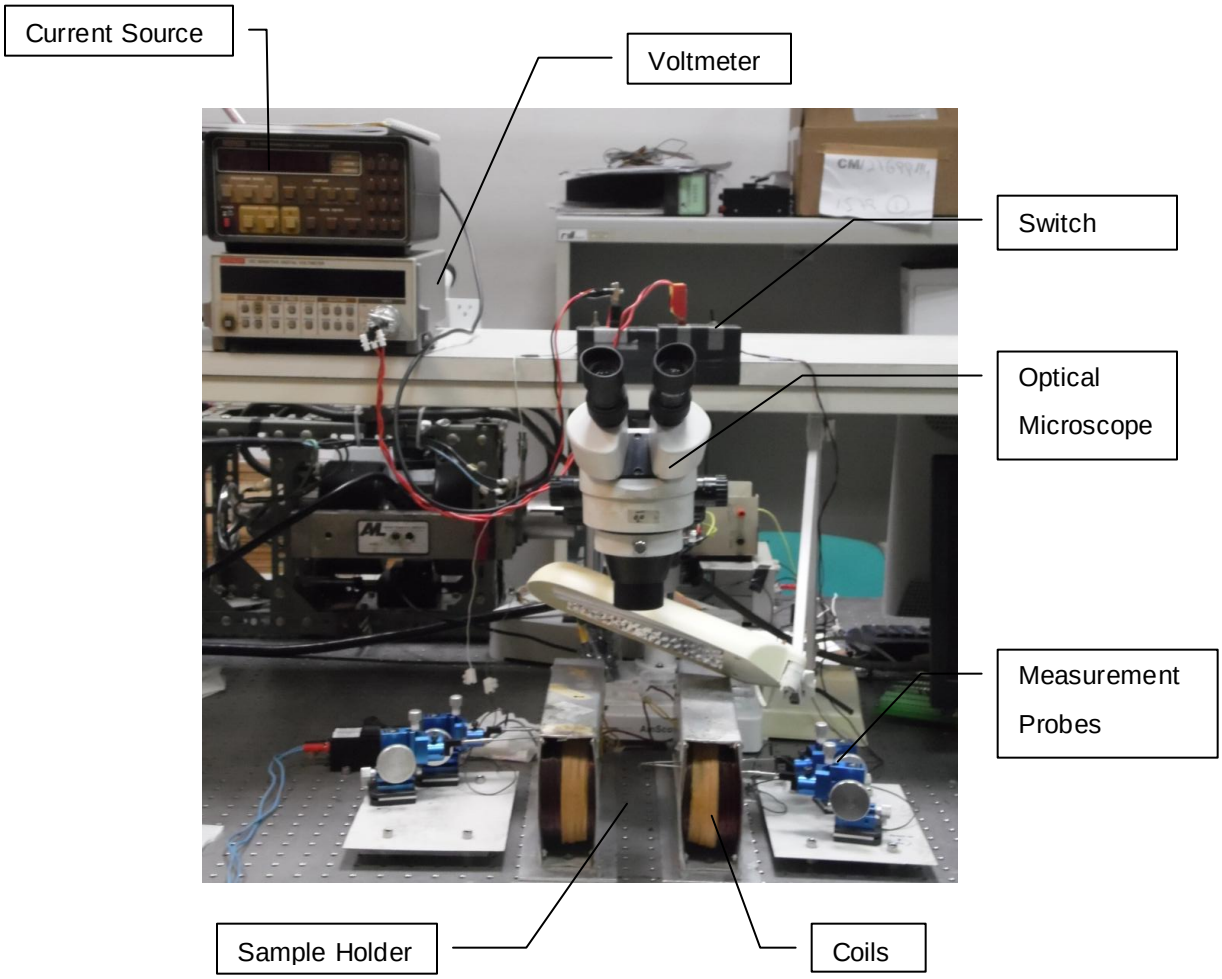

Figure 24 – MR setup in the Characterization Room at INESC-MN.

The resistance is measured using a current source (Keythley 220, with a range of 1 pA-100 mA) and a voltmeter (Keuthley 182). A GPIB (IEEE-488) bus controls the computer for data acquisition, the current supply, the voltmeter and the current supply fot the coils to create the external magnetic field. The current in the coils is set by a Kepco BOP 50-4 D current supply. The magnetic field is calibrated versus the coil current (using a external gaussmeter for the field measurement), and for a coil separation of 8 cm the maximum field of 140 Oe is measured at the sample area. The field uniformity is a must so the sample must be placed in the center of the two coils. A switch prevents electrostatic damage, by shutting the leads while the contact is being done to the sample.

The measurements are done after selecting the current to apply in order to have 5-10 mV voltage across the junction.

3 MTJ Stack Optimization

3.1 Electrodes Characterization

3.1.1 Compositional Characterization by RBS/PIXE analysis

The RBS data were analyzed with the IBA DataFurnace NDF v9.6a. [12]. Samples with 300 Å were deposited in silicon substrate and analyzed in RBS system in the *C²TN* (Centro de Ciências Tecnológicas e Nucleares). The PIXE results for the deposited samples were:

Table 6 – Ratio and composition from the RBS/PIXE analysis.

Sample	Ratio of Co/Fe	Composition
$Co_{70}Fe_{30}B_{20}$	2.4	$Co_{58}Fe_{42}B_{20}$
$Co_{90}Fe_{10}$	10.7	$Co_{91}Fe_{9}$

The values led to good fits as can be seen in the shape of the CoFe signal:

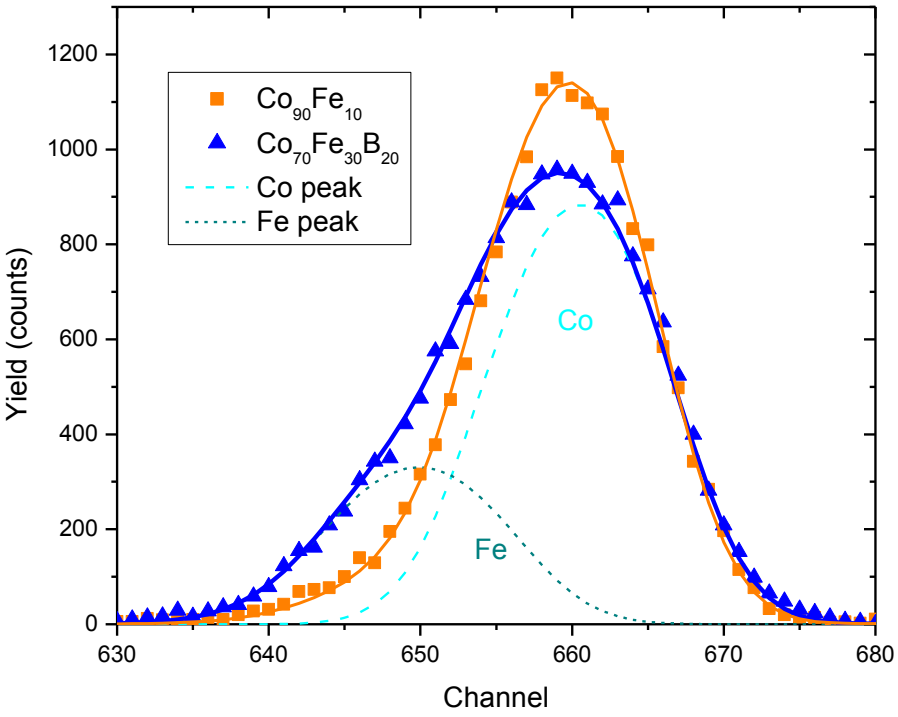

Figure 25 – RBS data from C²TN for the CoFe and CoFeB samples deposited in the Nordiko 3600.

For the $Co_{90}Fe_{10}$ corresponds the sharpest peak mostly due to Co. On the other hand the $Co_{70}Fe_{30}B_{20}$ corresponds to the broadest, corresponding to the highest Fe content.

3.1.2 Magnetic Characterization by VSM

The maximum possible magnetization or saturation magnetization M_s, of a ferromagnetic material represents the magnetization that results when all magnetic dipoles in a solid piece are mutually aligned with the external field [13]. The saturation is equal to the product of the net magnetic moment for each atom and the number of atoms present in the volume.

$$M_s = \mu_0 \times N$$

Where, the μ_0 is the number of Bohr magnetrons per atom and N the number of atoms per cubic meter. N is related to the density, ρ , the atomic weight, A , and the Avogadro's number, N_A, as follows:

$$N = \frac{\rho \ N_A}{A}$$

To obtain the theoretical values of the saturation magnetization for CoFe and CoFeB, the values for bulk Fe and Co were calculated and their weight % were taken into account to calculate an approximate value to M_s for the composition.

The numbers of Bohr magnetron for Fe and Co are 2.22 and 1.72, respectively. The values for N obtain for Fe and Co are $8.49 \times 10^{28}\ atoms/cm^3$ and $8.99 \times 10^{28}\ atoms/cm^3$ assuming $\rho_{Fe} = 7.87\ g/cm^3$ and $\rho_{Co} = 8.80\ g/cm^3$.

The values obtain for the saturation magnetization are presented in Table 7.

Table 7 – Magnetization Saturation of as deposited CoFe and CoFeB thin films. $\boldsymbol{Ms^T}$ was calculated considering $\boldsymbol{Co_{90}Fe_{10}}$ and $\boldsymbol{Co_{70}Fe_{30}B_{20}}$ compositions. $\boldsymbol{Ms^{RBS}}$ was calculated considering $\boldsymbol{Co_{91}Fe_9}$ and $\boldsymbol{Co_{58}Fe_{42}B_{20}}$ compositions.

Target	Magnetization Saturation (emu/cm^3)		
	$Ms^{VSM}\ (emu/cm^3)$	$Ms^T (emu/cm^3)$	$Ms^{RBS} (emu/cm^3)$
CoFe	1110 ± 98.7	1464.8	1461.64
CoFeB	904 ± 95.1	1222	1251.98

The VSM curves presented in Figure 26 are the magnetic response of as deposited CoFe and CoFeB films with a thickness of 300 Å. For both films a measurement in the easy axis and a measurement in the hard axis were preformed. The difference of the easy and hard axis measurement is on the angle at which the measurement is preformed: for easy axis the angle between direction of the field applied during the measurement and the field applied during deposition is 0 while for the hard axis this angle is 90 degrees.

For both materials the magnetic hysteresis curves have different shapes when easy and hard axes are plotted in Figure 26. This difference in shape is defined as magnetic anisotropy (or magnetocrystalline) and is intrinsically related to the crystallographic orientation of the

ferromagnetic thin films. Since easy axis represents the crystallographic direction in which magnetization is easiest, that is, saturation is achieved at the lowest *H* field. This is defined during the deposition a uniform field of 50 Oe is applied in order to define the easy axis. On the other hand, a hard crystallographic direction is that direction for which saturation magnetization is most difficult and thus a higher *H* field is needed to achieve saturation.

From Figure 26 the film coercivity can be determined and compared: $H_c^{CoFe} = 10.3\ Oe > H_c^{CoFeB} = 3.9\ Oe$. The higher coercivity observed in the CoFe is an indication of a higher grain size [14].

The lower Ms^{VSM} values are mainly due to two factors: the approximation used in the theoretical calculations and the dependence of the M_s on the thickness of the film. The theoretical values take into account the bulk values of perfect Co and Fe crystals and for an alloy of CoFe in thin film produced by Ion Beam Deposition defects. For thin films the interface interactions with the substrate and cap layer also have an impact in the M_s. However in both the $Ms^{CoFe} > Ms^{CoFeB}$. The M_s^{VSM} value for a $Co_{80}Fe_{20}B_{20}$ electrode was previously reported as 860 emu/cm^3 [15]. The value is within the error bar of the measurement, but the a lower value was expected due to the higher ratio of Co/Fe. Other groups have also achieved $M_s = 900\ \mathrm{emu/cm^3}$ for a 300 Å of $Co_{40}Fe_{40}B_{20}$ [16].

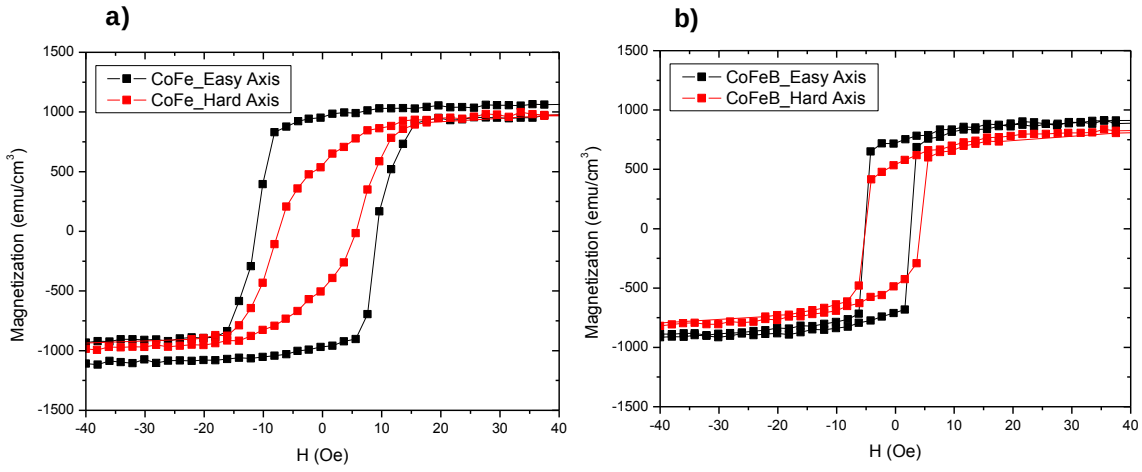

Figure 26 – VSM characterization of: a) Easy and Hard Axis of an as deposited 300 Å $\boldsymbol{Co_{90}Fe_{30}}$ Film. b) Easy and Hard Axis of an as deposited 300 Å $\boldsymbol{Co_{70}Fe_{30}B_{20}}$ Film.

Ferromagnetic materials are classified as either soft or hard on the basis of their hysteresis characteristics. A soft magnetic material is usually characterized by having a high initial permeability and a low coercivity, the latter is related to the easy movement of domain walls as the magnetic field changes magnitude and/or direction. The domain wall motion can be restricted by particles or structural defects. On the other hand hard magnetic materials are characterized by having a high coercivity and low initial permeability.

In comparison to the CoFeB the CoFe is a harder magnet, which is something to be expected. The Boron is used in the CoFeB alloys in order to grow the CoFe films in an amorphous phase. It is known that for concentrations higher than 15 at.% in Boron the CoFeB alloys are amorphous

and have a lower M_s [17]. Furthermore, the 20 at.% was found to have the higher tunnel spin polarization and higher TMR and lower RxA were also found for the 20 at. % when compare to 25 and 30 at.% [17] [18].

3.2 Pinned Layer by AFM/FM Exchange Bias

TMR measurements require the measurement of the resistance of the MTJ pillar with electrode in both parallel and antiparallel configurations as stated in 1.2.1. In order to obtain both configurations one of the electrodes' magnetization is fixed, and is usually referred as Pinned Layer. On the other hand the other electrodes' magnetization will change depending on the direction of the applied external field, often referred as Free Layer.

The aim of the study presented in this chapter is to achieve a configuration where a Pinned Layer with values of $H_E > 250\ Oe$ and $H_c < 50\ Oe$. These values were estimated in order for the MR transfer curves measured (setup described in 2.5) show the resistance of the parallel and antiparallel configuration. This implies the full saturation of both the Free and Pinned Layer in both parallel and antiparallel configurations with an external applied field with a range from -140 to 140 Oe.

The exchange bias phenomena (described in section 1.1.1) can be used to "pin" a ferromagnetic layer and is a crucial step in the development of an MTJ stack. In the past several AFM/FM interfaces have been studied, detailed studies with MnRh/CoFe [19], MnIr/CoFe [19] and MnPt [20] have been carried out at INESC-MN.

In this study the exchange bias system is composed by a layer of CoFe grown on top of a 180 Å MnIr layer. The thickness was previously optimized taking into account the thermal stability. The blocking temperature for this thickness was determined to be of 240 °C, also reported by other groups [21] [22]. The magnetization curves were measured in the a VSM system (described in 2.2).

The exchange bias of a MnIr 180 Å/CoFe 60 Å is expected to change between 125 and 500 Oe, depending mainly on the annealing temperature and the seed layer [23]. Throughout this study the annealing step was kept constant at a 240°C during 30 minutes, however the influence of the seed layer material and thickness was studied in order to obtain the desired values of the H_E and H_c for the MnIr/CoFe system.

The composition for the MnIr target is also a critical variable in the exchange bias. The target nominal composition is $Mn_{80}Ir_{20}$, thus between the range of 16 to 20.5 at.% has been reported to show good values of H_E [24].

This study is divided in two parts, where each part corresponds to a specific target assembly. In Part I (3.2.1) a 5 target assembly, constituted by Ta, MnIr, CoFe, CoFeB and Al, was mounted in the Chamber of the Nordiko 3600. For the Part II (3.2.2) the Ta target was substituted by NiFeCr and a sixth target of Ru was added.

A basic configuration of the multilayer structure used in this study is shown in Table 8. The colors were attributed to each function and are kept constant throughout the results presentation and discussion. The Magnetization versus Applied Field graphic is presented on the right.

The first cell contains the sample name, the same as the one used in the process and in the graphic caption. Next cell corresponds to the color of the magnetic response of the sample shown in the graphic.

Table 8 - Color, representation and function of each layer in the multilayer stacks

Sample Name	
Cap Layer	Prevents oxidation of the structure during the sample preparation, annealing and measuring processes.
Pinned Layer	Ferromagnetic where a exchange bias should be observed.
Anti-Ferromagetic Layer	Anti-Ferromagnetic responsible to create the exchange bias.
Seed Layer	Responsible to promote the correct crystalline growth of the AF
Bottom Contact	Responsible for decreasing the resistance of the MTJ stack deposited.

3.2.1 Part I

Exchange bias values on the order of the 150 Oe were previously obtained with a Ta buffer layer in a Top Configuration in Nordiko 3600 system. Higher values where expected for a Bottom Configuration.

Both 30 and 100 Å of Ta seed layer were used, but no exchange bias was observed. More samples with similar configurations were deposited but the results do not add more relevant information. When the chamber was vented a hole was found in the target Ta due to deposition process. The hole in the target is a probable cause for the the MnIr/CoFe system to present no exchange bias with a Ta seed layer (Figure 26). The target hole has a different composition thus contaminating the Ta films and consequently creating a seed layer that does not help promoting growth of the fcc-(111) texture of the MnIr layer, a requirement to the exchange bias phenomena.

36c038	36c041
Ta 100Å	*Ta 100Å*
CoFe 30Å	*CoFe 30Å*
MnIr 180Å	*MnIr 180Å*
Ta 30Å	***Ta 100Å***

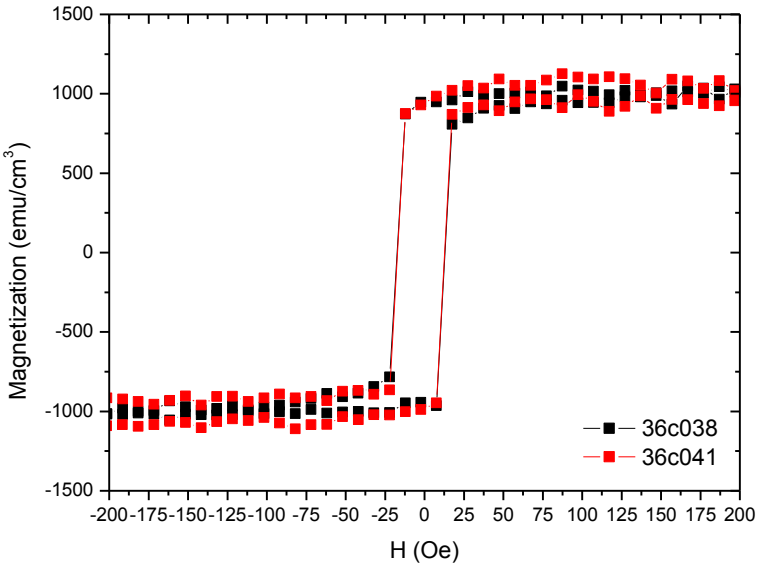

Figure 27 – VSM data for exchange bias study of MnIr/CoFe interface in a Ta seed layer deposited in the Nordiko 3600.

Figure 28 – Photograph from the Ta target surface showing a strong profile caused by the Ion Beam. The darker spot in the center is and epoxy polymer used to attach the 3 mm Ta plate to the target support.

36c042
Ta 100Å
CoFe 30Å
MnIr 180Å
CoFe 60Å
Ta 30Å

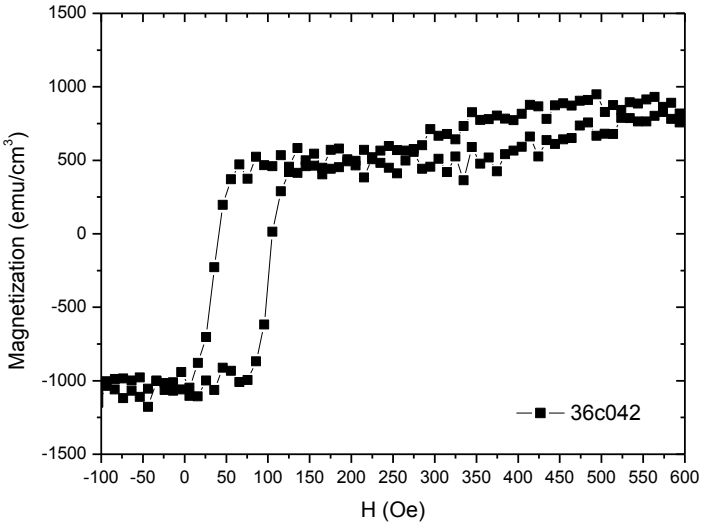

Figure 29 – VSM data for exchange bias study of MnIr/CoFe interface in a CoFe seed layer deposited in the Nordiko 3600.

Between the Ta and the MnIr a CoFe 60 Å layer was added resulting in a two step curve that can be observed in Figure 29. This is an expected outcome from this a "trilayer" stack [25] [26].

The exchange bias has been reported to be higher for bottom configuration than top configuration [23], thus a step with a $H_E = 68\ Oe$ corresponds to the seed layer of 60 Å CoFe and the other step corresponds to the Pinned Layer. This is also supported by the fact that the contribution to the magnetization saturation value is also higher for that step implying it to correspond to the ferromagnetic layer with higher thickness

Although the CoFe film promotes the desired growth of the MnIr fcc-(111) phase, its addition will create a fringe field (Hf), undesired magnetic field that will be responsible for a constant offset of the free layer rotation. The aim of the study was to reduce the thickness of the CoFe seed layer to minimize the contribution of this field but still promote the desired growth of the MnIr fcc-(111) phase.

36c057	36c058	36c059	36c060
Ta 100Å	*Ta 100Å*	*Ta 100Å*	*Ta 100Å*
CoFe 50Å	*CoFe 50Å*	*CoFe 50Å*	*CoFe 50Å*
MnIr 180Å	*MnIr 180Å*	*MnIr 180Å*	*MnIr 180Å*
CoFe 20Å	***CoFe 30Å***	***CoFe 40Å***	***CoFe 50Å***
Ta 30Å	*Ta 30Å*	*Ta 30Å*	*Ta 30Å*

.

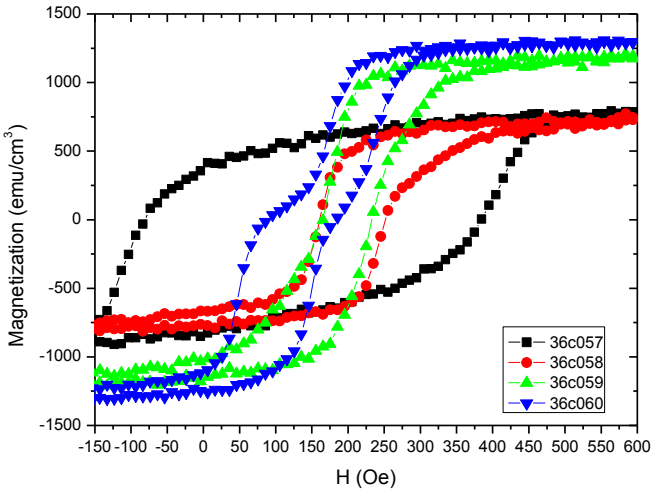

Figure 30 – VSM data showing the influence of the CoFe seed layer thickness on the exchange bias of the Pinned Layer.

A lower thickness of the CoFe seed layer showed a higher H_E for a 50 Å CoFe Pinned Layer. This series shows that the H_E of the seed layer is lower for higher thicknesses an can be related to $H_E \propto \frac{1}{t_{FM}}$ as shown in Figure 30.

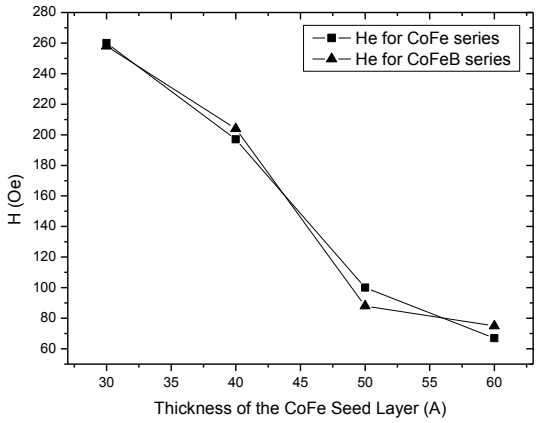

Figure 31 – Thickness dependence of the seed layer exchange bias as predicted by the theoretical model of the ideal interfaces.

A direct exchange bias between the MnIr and CoFeB was not obtained due to its amorphous phase. Exchange bias reported of 6 Oe has been reported for this interface but do not meet the requirements for the MTJ study [27]. However the CoFeB electrodes were an important aim of this study so a Pinned Layer of CoFeB was a requirement.

In order to obtain a CoFeB pinned Layer a 20 Å of CoFe layer was added between the MnIr and the CoFeB. This was expected to maintain the same coupling energy between the MnIr and the CoFe, while a new interface between two ferromagnets (CoFe/CoFeB) would behave as a single ferromagnetic layer. This was found to be true and the results obtain are presented in Figure 32.

36c061	**36c062**	**36c063**	**36c064**
Ta 100Å	*Ta 100Å*	*Ta 100Å*	*Ta 100Å*
CoFeB 30Å	*CoFeB 30Å*	*CoFeB 30Å*	*CoFeB 30Å*
CoFe 20Å	*CoFe 20Å*	*CoFe 20Å*	*CoFe 20Å*
MnIr 180Å	*MnIr 180Å*	*MnIr 180Å*	*MnIr 180Å*
CoFe 30Å	***CoFe 40Å***	***CoFe 50Å***	***CoFe 60Å***
Ta 30Å	*Ta 30Å*	*Ta 30Å*	*Ta 30Å*

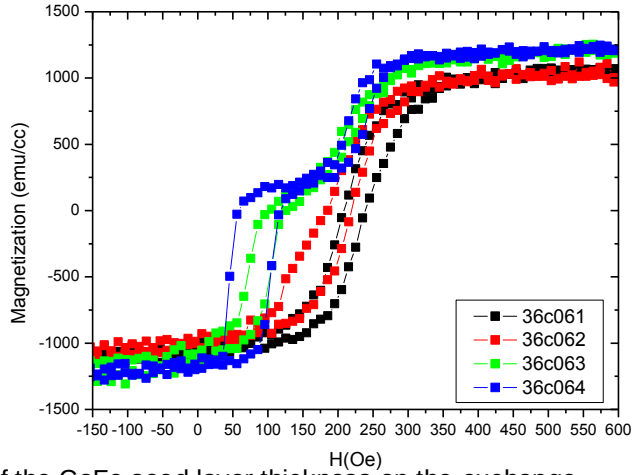

Figure 32 – VSM data showing the influence of the CoFe seed layer thickness on the exchange bias of the Pinned Layer (CoFe/CoFeB).

A similar behavior was observed regarding the seed and pinned layer. However the H_c values measured for the Pinned Layer were lower, the CoFeB layer was the main reason for this behavior. The 30 and 40Å seed layers of CoFe showed a behavior that meet the requirements

and thus a Bottom Electrode of Al 80 Å /Ta 30 Å was added and an impact on the H_E was observed (Figure 33 and Figure 33).

The results show that the Bottom Contact increased the exchange bias of the Pinned Layer, however a higher H_c was measured. This increase in H_c is mainly due to the increase in the roughness, not only due to the Ta target condition but also the Al thin films are known to have high values of roughness.

With the addition of the Al/Ta Bottom Electrode the stack with the 40 Å Pinned Layer a $H_c = 39\ Oe$ and a $H_E = 243\ Oe$ were measured. This hysteresis curve shows a behavior suitable for MTJ fabrication and measurement. For the 30 Å Pinned Layer a lower H_E and a higher H_c was observed.

36c061	**36c065**
Hc = 15 Oe	Hc = 52 Oe
Hex = 230 Oe	Hex = 235 Oe
Ta 100Å	*Ta 100Å*
CoFeB 30Å	*CoFeB 30Å*
CoFe 20Å	*CoFe 20Å*
MnIr 180Å	*MnIr 180Å*
CoFe 30Å	***CoFe 30Å***
Ta 30Å	*Ta 30Å*
	Al 80Å
	Ta 30Å
	Al 80Å
	Ta 30Å
	Al 80Å
	Ta 30Å
	Al 80Å
	Ta 50Å

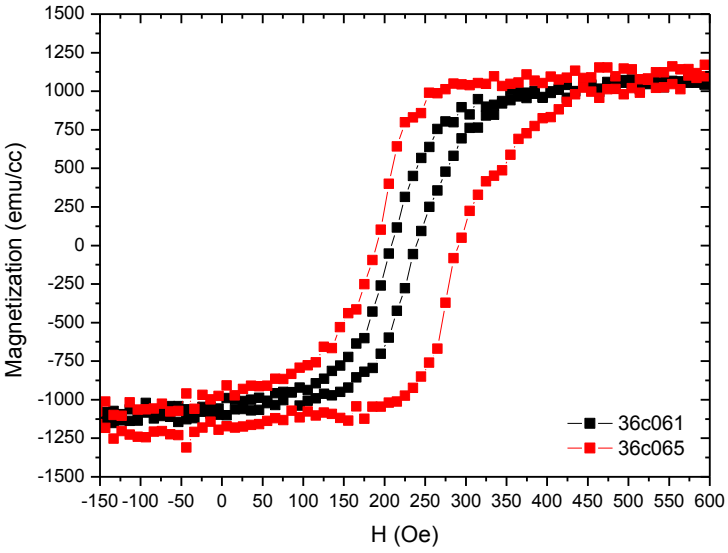

Figure 33 – VSM data showing the influence of an Al/Ta Bottom Contact on the exchange bias and coercivity of the Pinned Layer (CoFe/CoFeB) with a seed layer of 30 Å of CoFe.

36c062	**36c066**
Hc = 12 Oe	Hc = 39 Oe
Hex = 227 Oe	Hex = 243 Oe
Ta 100Å	*Ta 100Å*
CoFeB 30Å	*CoFeB 30Å*
CoFe 20Å	*CoFe 20Å*
MnIr 180Å	*MnIr 180Å*
CoFe 40Å	***CoFe 40Å***
Ta 30Å	*Ta 30Å*
	Al 80Å
	Ta 30Å
	Al 80Å
	Ta 30Å
	Al 80Å
	Ta 30Å
	Al 80Å
	Ta 50Å

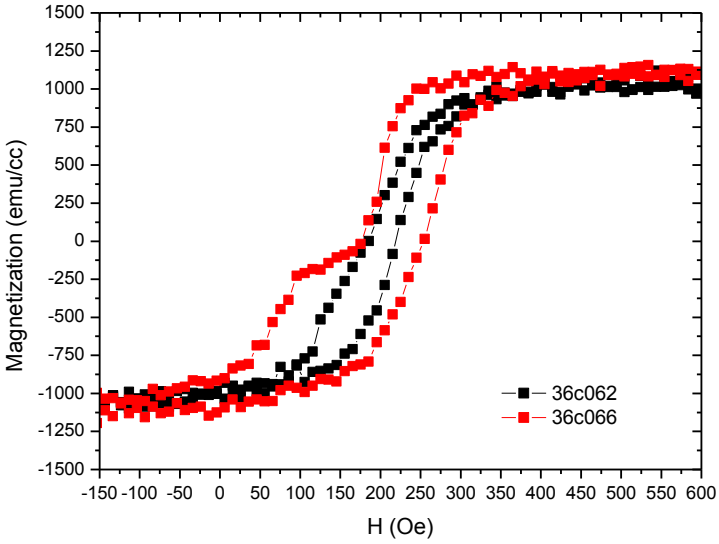

Figure 34 – VSM data showing the influence of an Al/Ta Bottom Contact on the exchange bias and coercivity of the Pinned Layer (CoFe/CoFeB) with a seed layer of 40 Å of CoFe.

3.2.2 Part II

The presented results were obtained by changing the thickness of the NiFeCr growth layer.

36c097	36c098	36c099	36c100
Hc = 257 Oe	Hc = 41 Oe	Hc = 41 Oe	Hc = 50 Oe
Hex = 163 Oe	Hex = 146 Oe	Hex = 146 Oe	Hex = 146 Oe
Ru 100Å	*Ru 100Å*	Ru 100Å	Ru 100Å
CoFe 50Å	*CoFe 50Å*	CoFe 50Å	CoFe 50Å
MnIr 180Å	*MnIr 180Å*	MnIr 180Å	MnIr 180Å
NiFeCr 20Å	***NiFeCr 30Å***	***NiFeCr 50Å***	***NiFeCr 100Å***

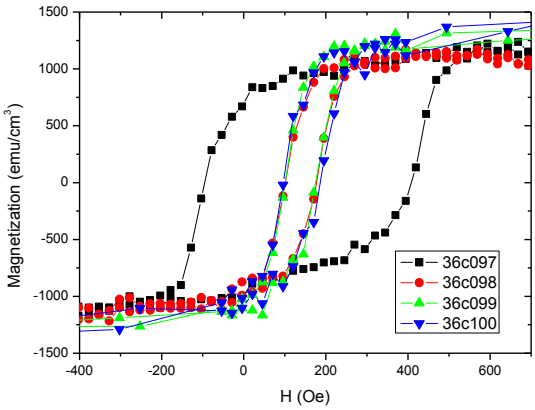

Figure 35 – VSM data showing the influence of the NiFeCr seed layer thickness on the exchange bias of the Pinned Layer (CoFe 50 Å).

For the studied values of the NiFeCr seed layer, the thickness seems to only affect the H_c while the H_E keeps constant at 150 Oe. Thus a thickness higher than 20 Å is required to obtain a good lower H_c.

The MnIr/CoFe was also grown without seed layer (on the glass substrate) and Ru. For the 50 Å of Ru the results meet the requirements for MTJ stacks with an exchange bias of 300 Oe and a coercivity of 19 Oe. The value is close the 295 Oe reported by Pakala. The results show a clear improvement with the addition of the Ru for the seed layer. The high exchange bias is due to the hcp (002) found in the Ru films that promotes the growth of the MnIr fcc (111) phase [23].

36c101	36c102
Hc = 236 Oe	Hc = 19 Oe
Hex = 194 Oe	Hex = 310 Oe
Ru 100Å	*Ru 100Å*
CoFe 50Å	*CoFe 50Å*
MnIr 180Å	*MnIr 180Å*
Glass	***Ru 50Å***

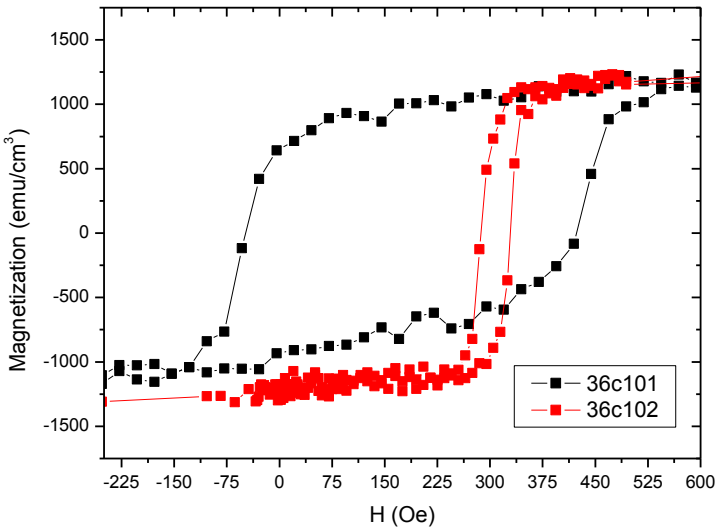

Figure 36 – VSM data showing the influence of an Al/Ta Bottom Contact on the exchange bias and coercivity of the Pinned Layer (CoFe/CoFeB) with a seed layer of 40 Å of CoFe.

This specific Bottom Electrode was found not to change the exchange bias nor the coercivity parameters significantly.

36c102	36c103
Hc = 19 Oe	Hc = 45 Oe
Hex = 310 Oe	Hex = 282 Oe
Ru 100Å	*Ru 100Å*
CoFe 50Å	*CoFe 50Å*
MnIr 180Å	*MnIr 180Å*
Ru 50Å	***Ru 50Å***
	NiFeCr 50Å
	Ru 150Å
	NiFeCr 50Å
	Ru 50Å

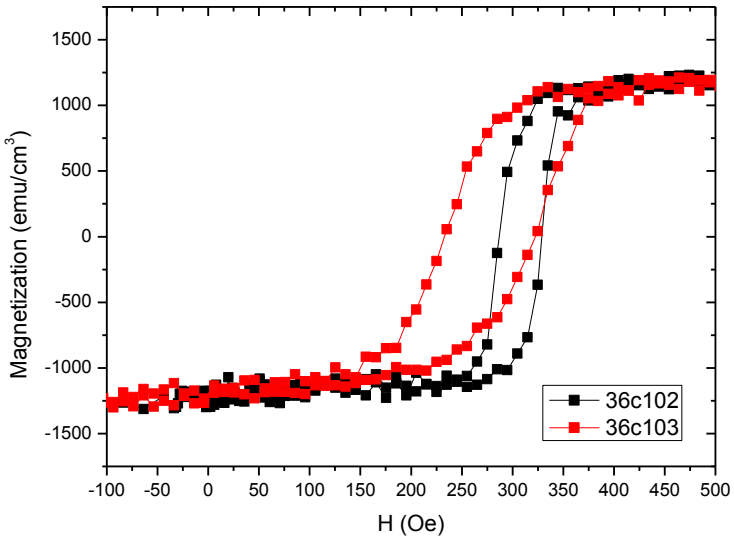

Figure 37 – VSM data showing the influence of an Al/Ta Bottom Contact on the exchange bias and coercivity of the Pinned Layer (CoFe/CoFeB) with a seed layer of 40 Å of CoFe.

The 36c103 shows no rotation of the pinned layer for fields between -140 and 140 Oe (range of the MR setup) which predicts this to be a good configuration to be used in MTJ process.

The increase in H_c can be correlated with the increase of roughness, while the linearization of the step can be caused by an angle between the sample and the field applied during the cooling step, an angle during the placement of the sample in the VSM setup or both.

A $\Delta\sigma = 0.17\ erg/cm^2$ was obtained for the Ru seed layer (obtained using a $M_s^{VSM} = 1110\ emu/cm^3$), very close to the value of $\Delta\sigma = 0.18\ erg/cm^2$ obtained by Pakala for the same system [23].

Pakala reports higher exchange bias for higher thicknesses of Ru (377 Oe for 400 Å), but also an increase of roughness (from 101 to 224 nm) which is expected to result in a higher H_c.

3.3 SAF with CoFe/Ru/CoFeB

The first evidence of antiferromagnetic coupling between two ferromagnetic layers, separated by a thin non-magnetic layer, was reported by Grünberg et al. in 1986. Since then several review papers on the interlayer exchange coupling and its theory see [28].

This approach to have a pinned layer of CoFeB with higher exchange bias was made possible by the insertion of the Ru on the Nordiko 3600 target assembly, since the Ru is widely used as a spacer for Synthetic Antiferromagnetic coupling between Ferromagnetic layers.

With a 30 minute at 240 °C annealing step a 1000 Oe exchange was obtained using a *CoFe 30Å* /Ru *9.2Å* / *CoFeB 30Å* system.

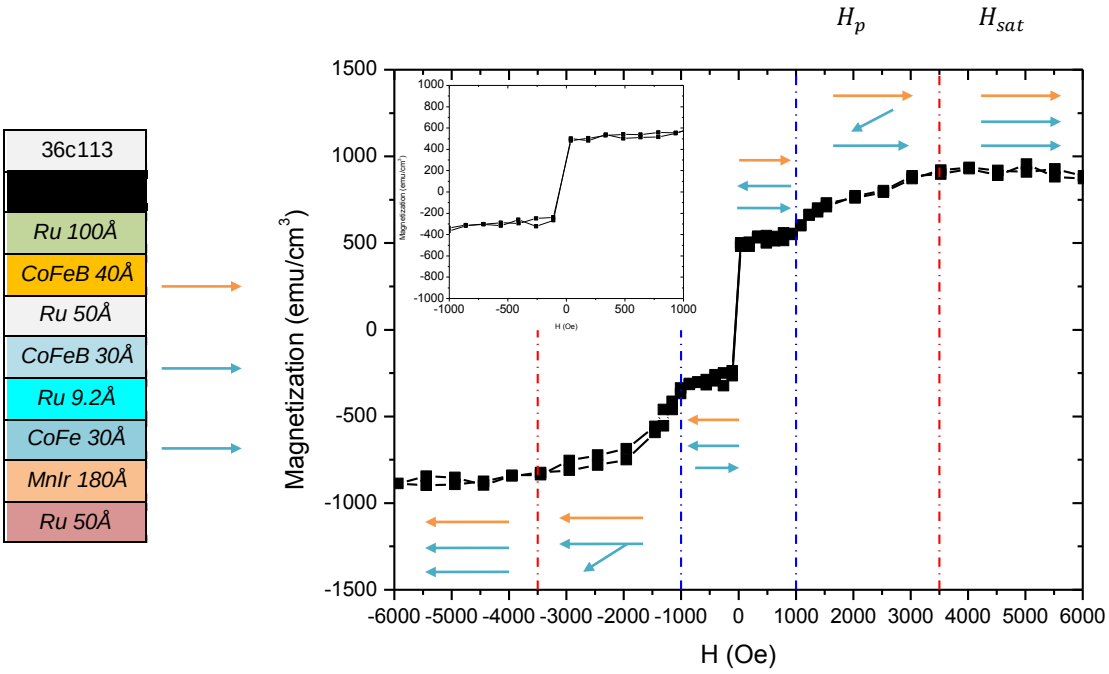

Figure 38 – VSM data showing a SAF of CoFe/Ru/CoFeB with a 30 minutes at 240°C annealing. The blue dashed ($\boldsymbol{H_p}$) line corresponds to the limits regime where the SAF of CoFe/Ru/CoFeB is in antiparallel state. The red dashed line represents the saturation field ($\boldsymbol{H_{sat}}$). The left top graphic shows the magnetic response of the 36c113 between -1000 Oe and 1000 Oe.

For large applied magnetic fields both ferromagnetic layers of the SAF are align ($H \geq H_{sat}$). For $H_p \leq H \leq H_{sat}$ the CoFeB begin to rotate from 0 deg to 180 deg, where the antiferromagnetic alignment is established at the plateau (H_p) value is reached. Near $H = 0$ the Free Layer rotates and thus the parallel and antiparallel configurations are achieved between the CoFeB below and over the barrier optimal to measure the TMR value.

4 Magnetic Dead Layer Study

Ultrathin ferromagnetic films are key constituents of the film stacks used in magnetic sensors and memory elements. With the decrease of the thickness of the ferromagnetic layer, the interfaces have a higher importance in the magnetic behavior of the thin films. The magnetic dead layers (MLD) refer to atomic layers that carry no magnetic moment and hence are non-magnetic even though the underlying bulk material is magnetic. These layers may form during deposition processes in the order of a few monolayers due to interface diffusion which causes magnetic moment loss of FM electrode. The magnetic moment can be written as:

$$m = \mu_B (D - D_{dead})$$

Where D is the thickness of magnetic material and D_{dead} is the thickness of layers that have no magnetic contribution to the magnetic moment.

In order to determine the number of dead layers, a series of electrode/barrier multilayer stacks was produced. The barrier was produced by plasma oxidation. The ferromagnetic materials used were the CoFe and the CoFeB described in 3.1.

In this study the thickness of the layer was decreased until a minimum of 10 Å, however a 10 Å layer represents a very low magnetic volume and thus a higher error and noise in the VSM measurements. In order to eliminate that source of error the total thickness of the magnetic material was kept constant and equal to 300 Å. This means that for studying a 10 Å layer, 30 layers of 10 Å were deposited with the barrier in between. In the same way multilayers with magnetic layer of 60, 30 and 15 Å were deposited. The sample names were given taking into account the number of aluminum oxide layers present in the stack (30 layers of 10 Å of CoFeB means we need 29 aluminum oxide barriers to separate them, thus n=29).

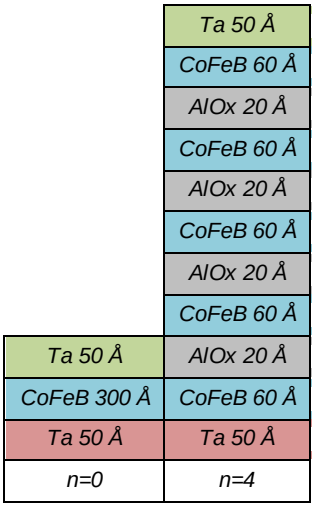

Figure 39 – Schematic of the Dead Layer study.

Table 9 – Table presenting the samples included in the Dead Layer Study.

Number of barrier layers (n)	Thickness of a single layer of magnetic material (t_m)
0	300 Å
4	60 Å
9	30 Å
19	15 Å
29	10 Å

Evolution of FM of thin films during deposition is an important factor to understand the formation of the non magnetic layers that form at interfaces. The evolution of magnetic phases of Fe films on GaAs at room temperature has been modeled by Xu in 1998 [29].

Examining hysteresis loops of Fe with different thickness gives an idea about the evolution of the films. The lack of magnetic signal for the first 3.5 Magnetic Layers (ML) for the Fe thin film is due to small cluster size of Fe which is not thick enough to construct a magnetic ordering. The magnetic signal comes from the thick Fe sample that shows good magnetic ordering. Thin Fe layer behaves as superparamagnetic and then non magnetic signal comes out due to irregular ordering of magnetic moment in the sample.

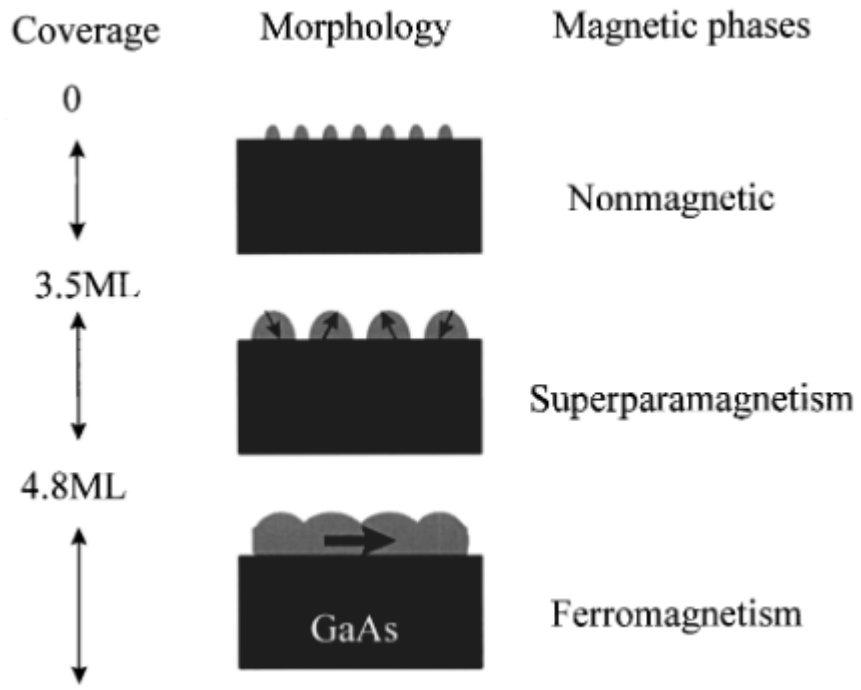

Figure 40 – Correlation between the coverage, morphology, and magnetic phases of Fe films on GaAs (001) substrate grown at room temperature ***[29]***.

Besides the deposition and growth of thin films on the magnetic dead layers the interdiffusion also plays dominant role for reducing magnetic moment of ferromagnets in magnetic tunnel junctions and reducing spin polarization of electrodes. Due to interdiffusion the thickness of the MDLs usually increases with annealing treatments.

4.1.1 Data treatment

The determination of MDL in this study is done in two steps. The first is to plot the VSM data and extracting the value of M_s (Figure 40 a)) for the multilayer series (from n=4 to n=29).

In order to determine the value of MLD found in the interface of electrode/barrier the values of M_s extracted from the VSM data were divided by the number of layers of magnetic material in the multilayer sample. The values of M_s per layer are then plotted against the thickness of a single layer (Figure 40 b)). Next the extracted values are fitted into a linear regression. The point where M_s per layer is 0 corresponds to an approximate value of the thickness of dead layers per magnetic layer. In order to obtain the number of dead layers per interface the value obtained for the linear fit has to be divided by the two interfaces of the magnetic layer with the barrier.

The dashed line in Figure 40 b) shows an example of a system where there are no dead layers.

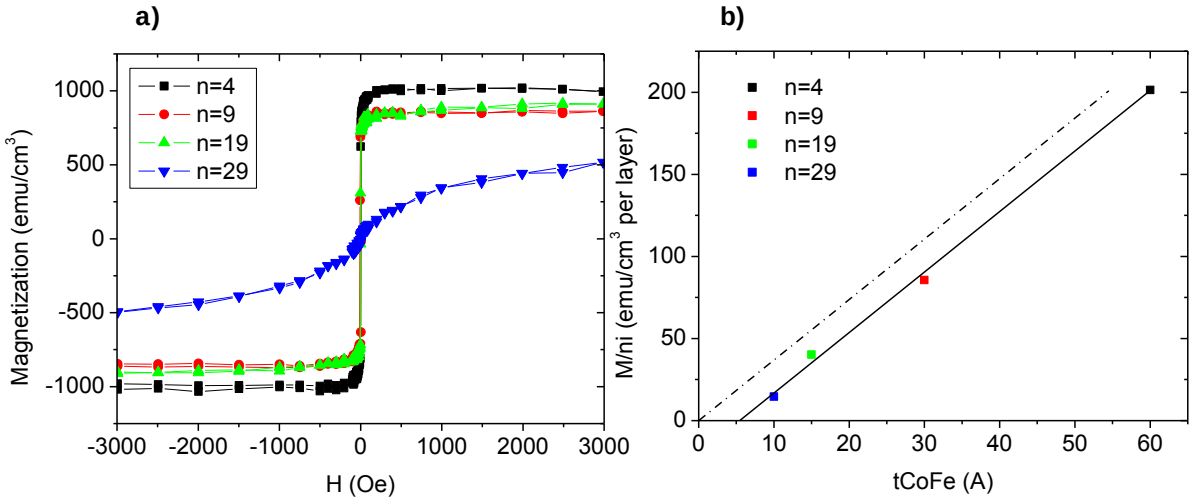

Figure 41 – a) VSM data for the Dead Layer study. Comparison between n=4 to n=29 multilayers (as deposited); b) Magnetic moment saturation per layer plotted against the thickness of a single layer.

4.1.2 Discussion

For each sample four VSM measurements were performed at different annealing steps. The chosen temperatures range from 200 to 300 °C and a 30 minute step duration.

4.1.2.1 CoFe

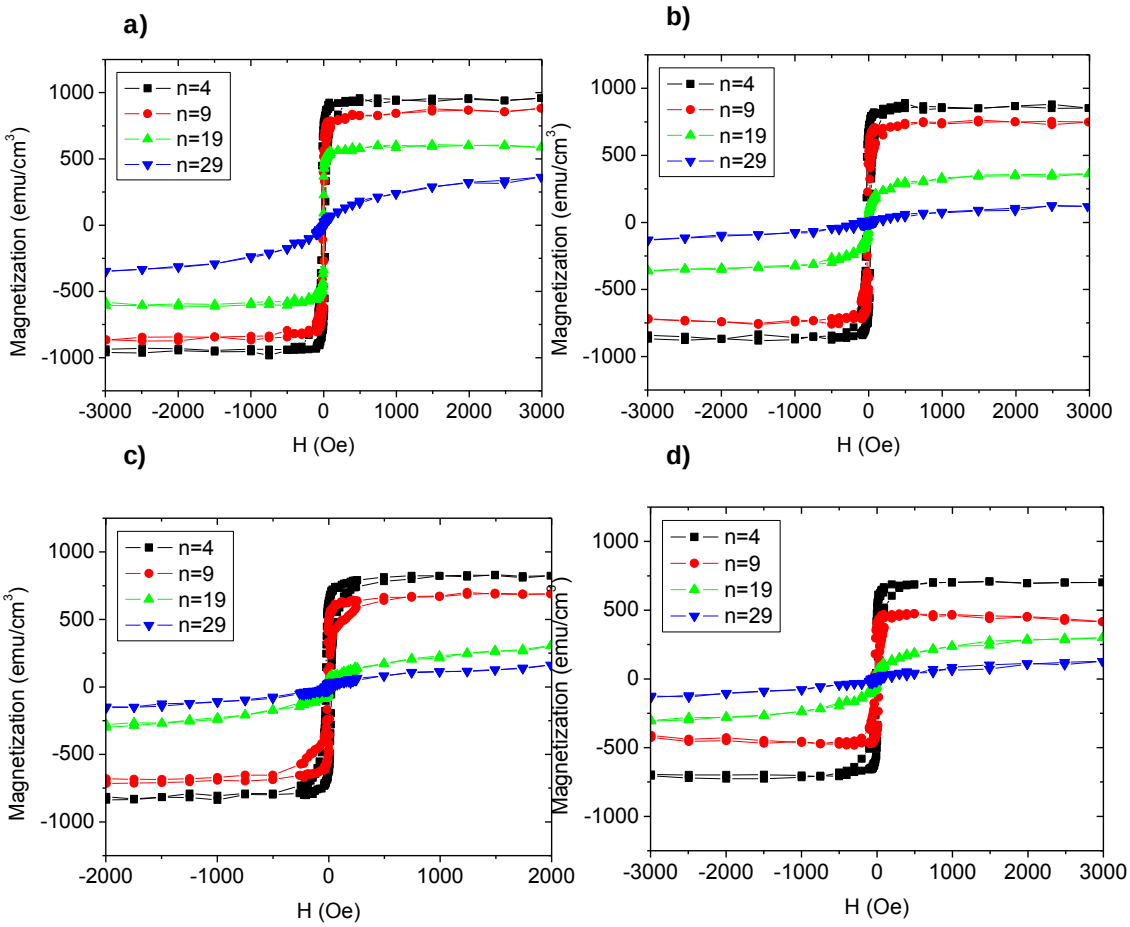

Figure 42 – Evolution of the magnetic moment for CoFe multilayer stacks with the annealing temperature: a) As deposited; b) 200°C; c) 250 °C; d) 300 °C

Figure 42 a) shows a paramagnetic behavior for the multilayers of 10 Å and a reduction of the M_s with the decrease of the single layer thickness. After an annealing of 200 °C only a diamagnetic contribution was observed probably due to the glass substrate, the silica rod and the thin films deposited.

The increasing annealing temperature lowers the M_s mostly due to the interdiffusion between the CoFe/AlOx interfaces. In the particular case of the multilayers of 15 Å (n=19) the interdiffusion has an important role in the magnetic response since there is a transition between ferromagnetic to paramagnetic behavior. This is probably due to the propagation of dead layer leaving small regions of ferromagnetic CoFe that will have a paramagnetic behavior.

4.1.2.2 CoFeB

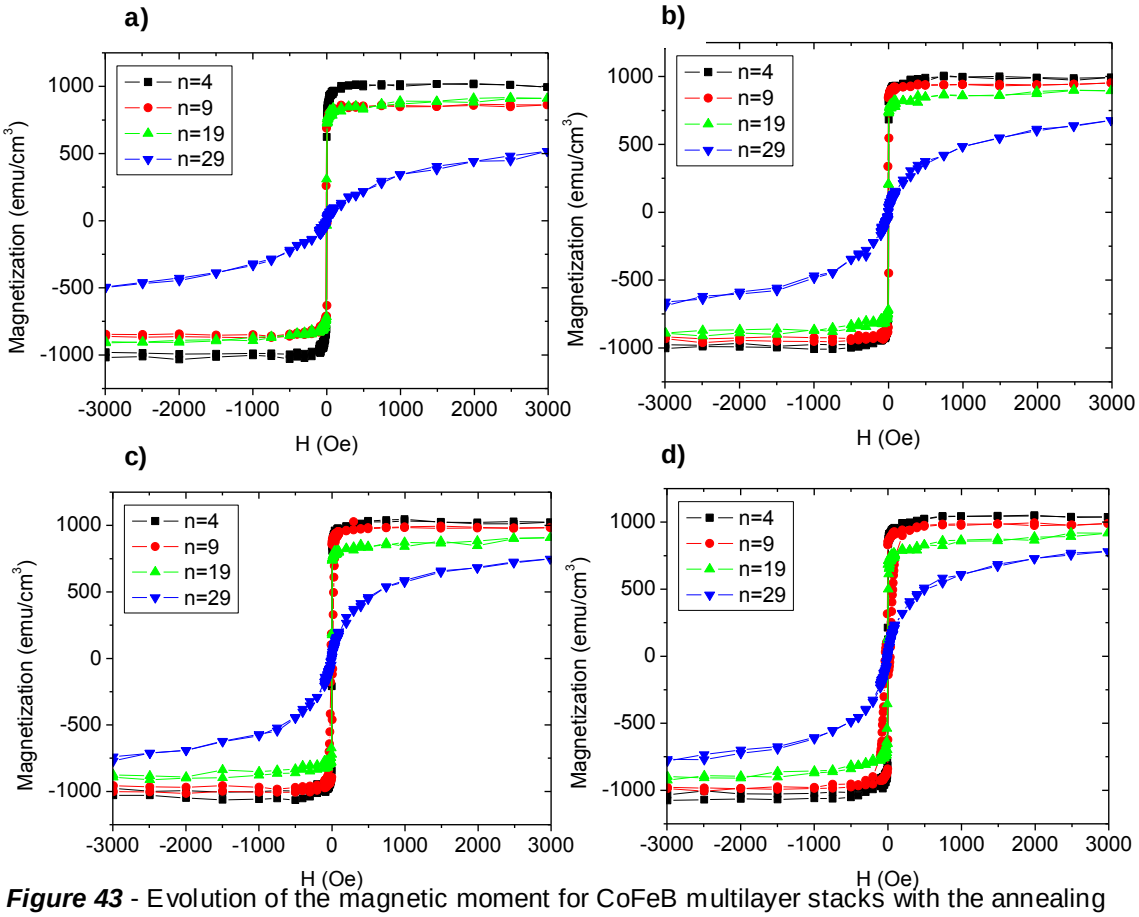

Figure 43 - Evolution of the magnetic moment for CoFeB multilayer stacks with the annealing temperature: a) As deposited; b) 200 °C; c) 250 °C; d) 300 °C

A different behavior was observed for the CoFeB multilayer study. Instead of a decrease in M_s the CoFeB series shows an increase clearly visible in the 10 Å multilayers sample (n=29). As deposited the hysteresis curve shows a paramagnetic behavior, however this behavior is modified with the annealing showing an evolution to a ferromagnetic response.

The changes in the hysteresis loops shown with the annealing temperature are probably due to the Boron diffusion, which is mainly driven by the crystallization of the CoFeB. The phase transition will have an impact in the M_s value and thus justifying its increase.

For CoFeB and CoFe electrodes the evolution with temperature can be observed in Figure 43. The evolution with temperature is clear for the CoFe (Figure 43 b)) since higher annealing results in a lower Ms per layer value and thus in a higher number of MDL.

For each temperature a linear fit was preformed the magnetically dead thickness of material was determined and the influence of the annealing temperature can be observed in Figure 44.

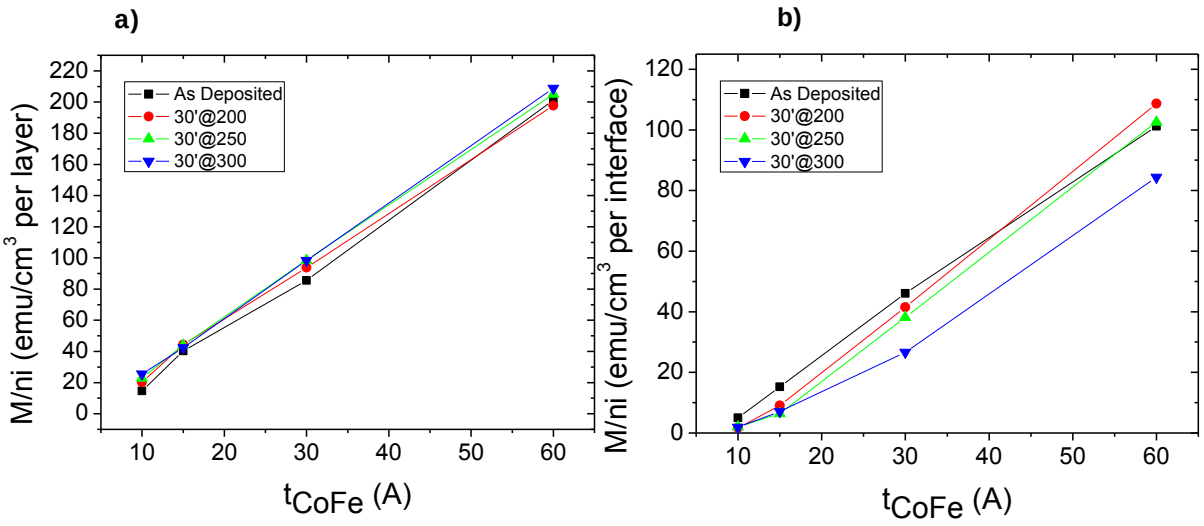

Figure 44 -) Magnetization per layer versus the thickness of a single layer for the CoFeB series; b) Magnetization per layer versus the thickness of a single layer for the CoFe series.

.

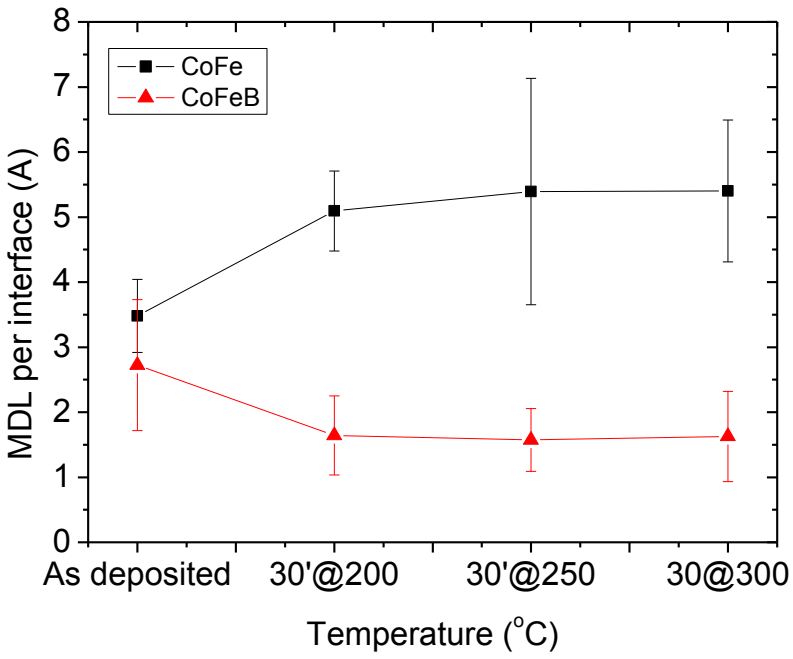

Figure 45 – Influence of the annealing temperature on the thickness of MLD (Magnetic Dead Layers) per Electrode/Barrier interface.

A clear reduction of the M_s per layer with annealing temperature can be observed from 250 °C to 300 °C in Figure 43 b) this would predict an increase of the MDL per interface. However this is not the case when the curve is fitted to linear and the results of MDL per interface are compared (Figure 44). This is due to the 10 Å sample that has a M_s value very close to 0 and thus is shifting the linear regression to a lower value of MDL (close to 10 Å), when in reality is a higher value. This is very clear when for CoFe multilayer samples annealed at 250 °C (see Figure 45).

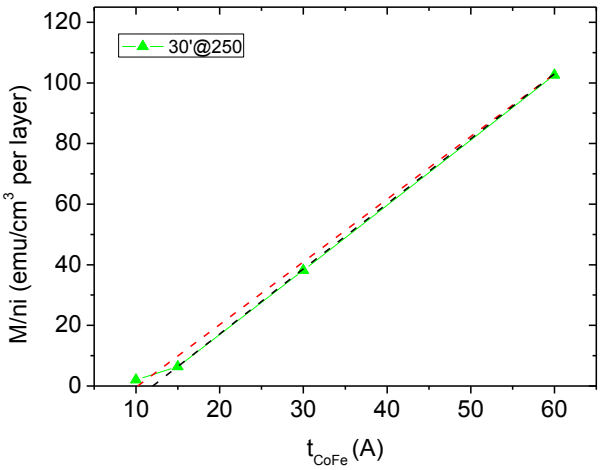

Figure 46 – Correction of the linear regression for the MLD determination by removing the 10 Å multilayer contributions. The red dashed line is the linear regression that takes into account the 10 Å layer. The black dashed line is the corrected linear regression.

The same correction was preformed for the samples annealed at 300°C. The results of the MDL that take into account the correction are presented in

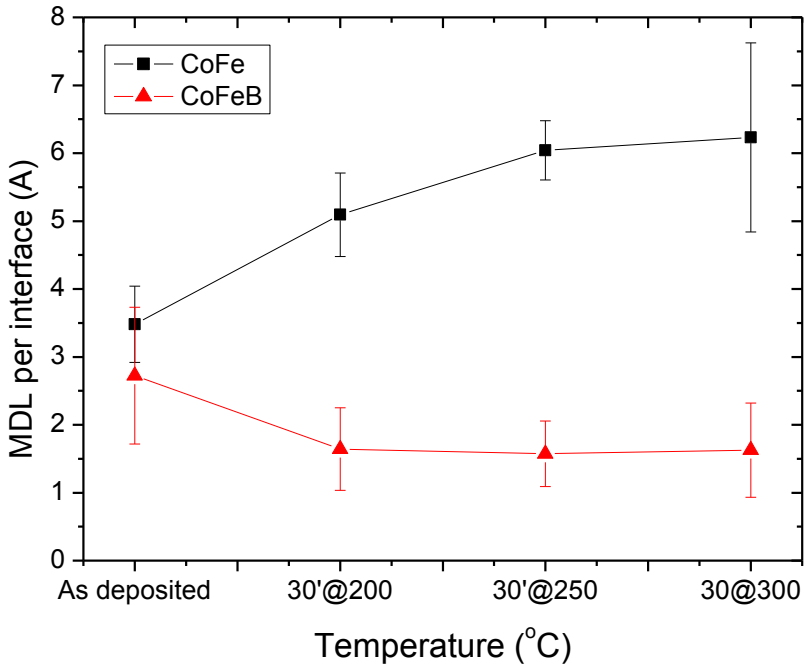

Figure 47 - Influence of the annealing temperature on the thickness of MLD (Magnetic Dead Layers) per Electrode/Barrier interface with correction.

5 Aluminum Oxide Barrier

Aluminum oxide is one of the most commonly used insulating barriers materials in MTJs because it is relatively easy to prepare and has a less costs associated with the process. The techniques used to prepare the aluminum oxide layers can be divided in two main groups, Plasma and non-plasma oxidation. The plasma techniques are usually related to higher RxA and TMR values with a record value for Plasma Oxidation of 70% TMR with an RxA of 24 $M\Omega.\mu m^2$ [7]. However for some application high RxA is a non desirable attribute. For this reason other techniques (non plasma) are used to obtain oxides with lower values of RxA such as: Thermal and Natural Oxidation.

5.1 Natural Oxidation

In order to create junctions with lower specific resistances, thinner barriers have to be produced. For oxidation of Al layers of 10 Å by plasma oxidation is no longer a good method manly because is thought to be too aggressive, possibly resulting in damage to the bottom electrode. Therefore, for thin barriers often thermal and natural oxidation is successfully used.

Natural Oxidation is often used to describe a process preformed at RT where a pure aluminum layer is in contact with an atmosphere where oxygen is present. The atmosphere can be controlled atmosphere (usually a pure oxygen atmosphere) or it can be air (sometimes referred as in situ natural oxidation).

From Figure 48 can be observed that for 8 hours of exposure time the barrier is still not fully oxidized. It is not surprising for the resistance to increase with exposure time, however the time required for oxidation process using natural oxidation becomes very long.

For Thermal Oxidation the same concept as Natural Oxidation with the fact that the oxidation step is preformed at a temperature higher than 50°C. This is a widely used method to reduce the oxidation time needed to produce the barriers with good TMR values.

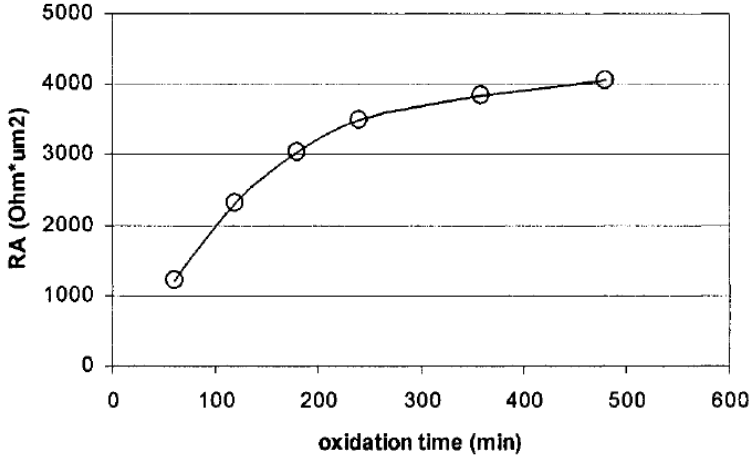

Figure 48 – The resistance-area (RA) product of a magnetic junction with 1.2 nm thick aluminum layer as a function of the exposure time to ambient air. ***[30]***

With CoFe electrodes and an aluminum oxide barrier:

- for a 7 Å barrier produced by natural oxidation in situ oxidation a TMR from 15% to 30% and an RxA from 10 to 70 $\Omega.\mu m^2$ has been reported by Wang at INESC-MN in the Nordiko 2000 machine. The range of values is related to the atmosphere pressure and time of exposition of the aluminum oxide barrier [31]; for a 9 Å barrier produced by natural oxidation of pure aluminum at air a 7.9% TMR and a 9.5 $\Omega.\mu m^2$ were reported [32] .

More interesting was the attempt made by Moon performing a two step oxidation. This means he deposited a 5 Å pure aluminum film followed by a natural oxidation step of 30 minutes and then 4 Å Al oxidized the same conditions. This allowed him to obtain a respectable 30% TMR with an 180 $\Omega.\mu m^2$ [32]. These results shows a clear improve in the tunneling properties of the aluminum oxide much due to the improvement in uniformity observed.

This chapter contains results from TMR and RxA measurements of patterned MTJ stacks with aluminum oxide barrier. The stack in Figure 49 is composed by the Bottom Contact the barrier produced by natural oxidation and the Free Layer. In this study the oxidation step was kept constant at 30 minutes of oxidation, while the thickness of the pure aluminum layer was changed from 5 Å to 11Å.

Two series with different materials in the electrodes CoFeB and CoFe were processed and measured in the 140 Oe MR setup.

NO_34	NO_35	NO_36	NO_37
Ru 100Å	Ru 100Å	Ru 100Å	Ru 100Å
CoFeB 40Å	CoFeB 40Å	CoFeB 40Å	CoFeB 40Å
AlOx 6Å	AlOx 9Å	AlOx 12Å	AlOx 14Å
Al 5Å	Al 7Å	Al 9Å	Al 11Å
CoFeB 30Å	CoFeB 30Å	CoFeB 30Å	CoFeB 30Å
Ru 9.2Å	Ru 9.2Å	Ru 9.2Å	Ru 9.2Å
CoFe 30Å	CoFe 30Å	CoFe 30Å	CoFe 30Å
MnIr 180Å	MnIr 180Å	MnIr 180Å	MnIr 180Å
Ru 50Å	Ru 50Å	Ru 50Å	Ru 50Å
NiFeCr 50Å	NiFeCr 50Å	NiFeCr 50Å	NiFeCr 50Å
Ru 150Å	Ru 150Å	Ru 150Å	Ru 150Å
NiFeCr 50Å	NiFeCr 50Å	NiFeCr 50Å	NiFeCr 50Å
Ru 50Å	Ru 50Å	Ru 50Å	Ru 50Å

NO_34	NO_35	NO_36	NO_37
Ru 100Å	Ru 100Å	Ru 100Å	Ru 100Å
CoFeB 40Å	CoFeB 40Å	CoFeB 40Å	CoFeB 40Å
AlOx 6Å	AlOx 9Å	AlOx 12Å	AlOx 14Å
CoFeB 30Å	CoFeB 30Å	CoFeB 30Å	CoFeB 30Å
Ru 9.2Å	Ru 9.2Å	Ru 9.2Å	Ru 9.2Å
CoFe 30Å	CoFe 30Å	CoFe 30Å	CoFe 30Å
MnIr 180Å	MnIr 180Å	MnIr 180Å	MnIr 180Å
Ru 50Å	Ru 50Å	Ru 50Å	Ru 50Å
NiFeCr 50Å	NiFeCr 50Å	NiFeCr 50Å	NiFeCr 50Å
Ru 150Å	Ru 150Å	Ru 150Å	Ru 150Å
NiFeCr 50Å	NiFeCr 50Å	NiFeCr 50Å	NiFeCr 50Å
Ru 50Å	Ru 50Å	Ru 50Å	Ru 50Å

Figure 49 – a) Schematic for the AlOx barrier production method; b) Full stack composition.

5.2 MTJ with AlOx Barrier

5.2.1 VSM Measurements

A measurement from -6 000 Oe to 6000 Oe shows the stack is working correctly. As expected the four stack show a very similar magnetic response, the small M_s differences are attribute to the method used to calculate the magnetic volume of the thin films.

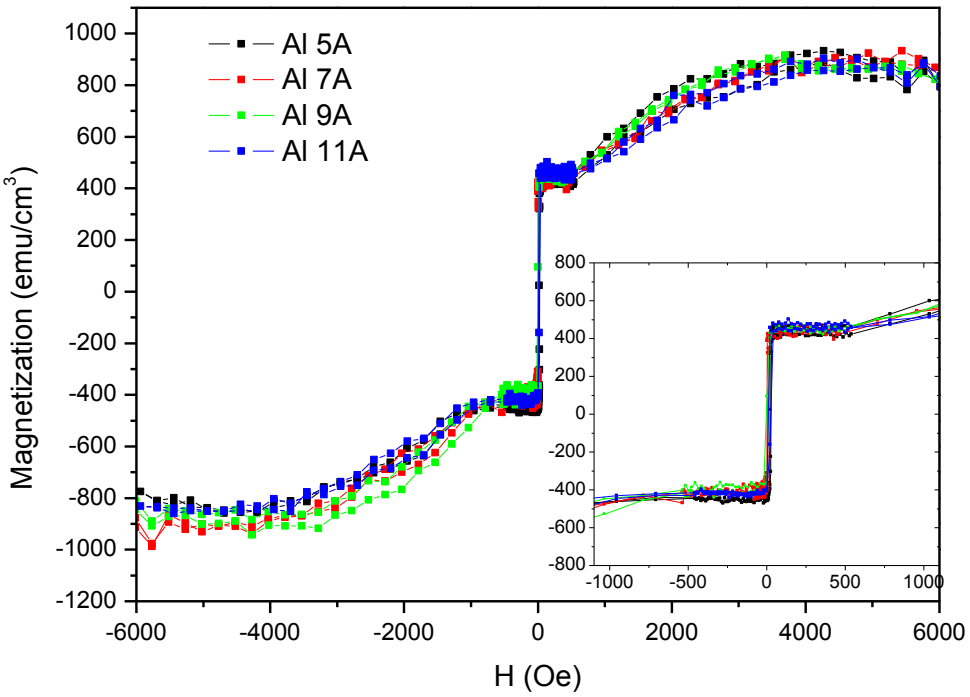

Figure 50 – VSM data showing identical and controlled magnetic response for the MTJ stacks

A measurement from -50 to 50 Oe was performed in order to measure coercivity and the coupling field between the Free and Pinned Layer.

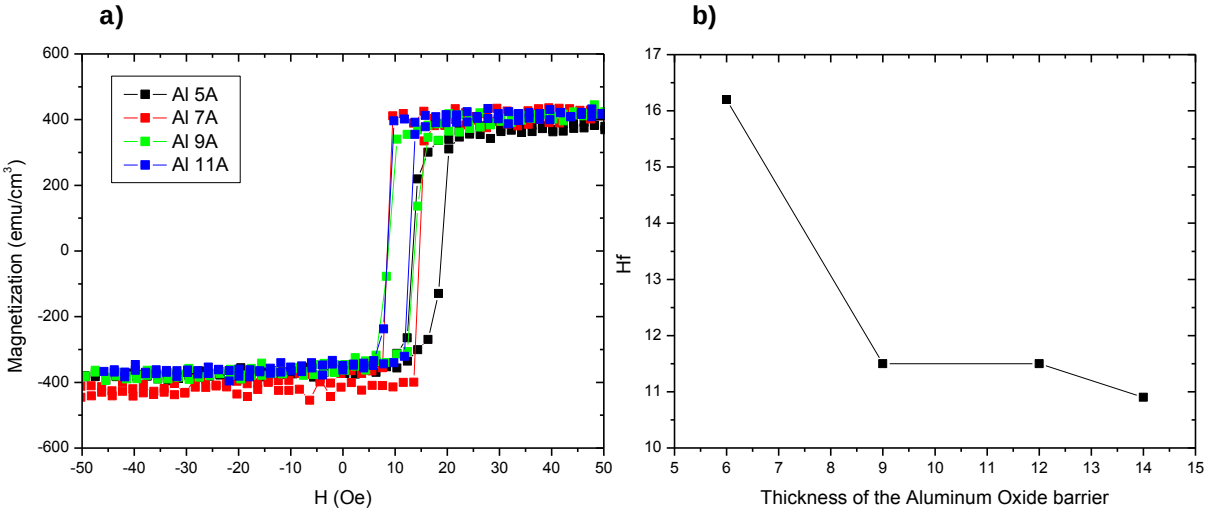

Figure 51 – a) VSM data showing a constant magnetic response of the free layer; b) the coupling field (Hf) as a function of thickness of the aluminum oxide barrier.

The values of coupling are low and on the order of magnitude previously reported, where barriers of 6 Å have a coupling field (H_f) of 10 Oe [31].

The H_f value is an important value in the characterization of the MTJ structures, not only for sensors but also for the memory application. This value measures the offset of the hysteresis curve of the Free Layer usually caused by the Fringe Field of the Pinned Layer and Neél Coupling phenomena.

5.2.2 TMR and RxA measurements

5.2.2.1 Data treatment

In this series the measurements showed problems regarding the processing. In order to explain what type of treatment the data was subjected to the raw data of the NO_34 sample is shown in Figure 52.

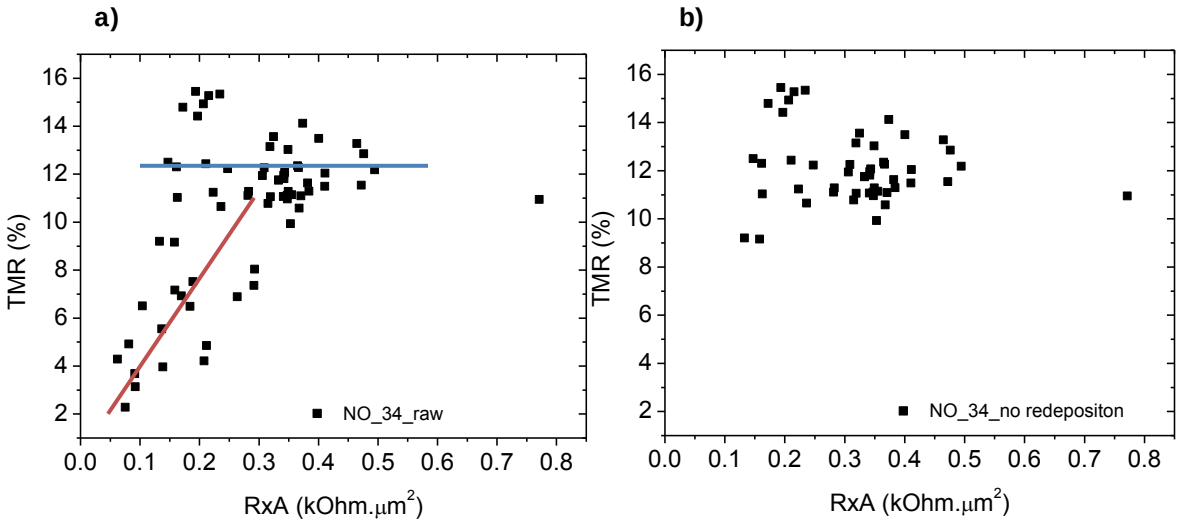

Figure 52 – a) NO_34 raw data b) NO_34 without the redeposition effect contribution.

As can be observed from the Figure 52 a) two tails can be identified: a linear response between TMR and RxA (red line); a constant TMR response with different RxA values (blue line).

The effect identified by the red line corresponds to redeposition material on the pillar's wall during the pillar definition step. Its contribution is removed in the Figure 52 b).

The redeposition effect happens in the pillar definition. Redeposition of conductive material on the sidewalls of the tunnel junction drives to a decreasing of tunneling transport across the barrier reducing the TMR signal. [33]

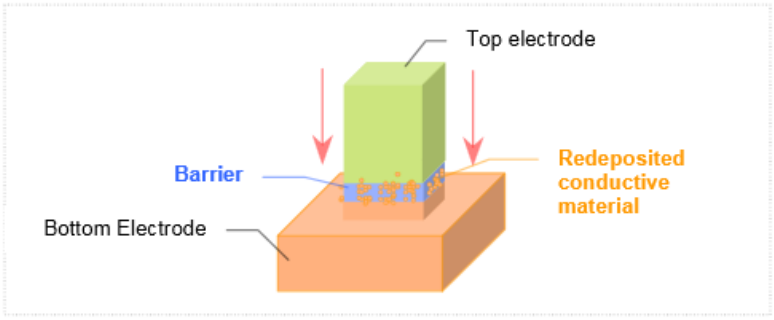

Figure 53 – Schematic of a tunnel junction in the second etch with material redeposition (orange spots) on the sidewalls, shorting parts of the barrier. ***[33]***

The broad spectrum of RxA (blue line) is related to poor control on the pillar area effective sizes. There are two main causes, one is the poor control of the nominal sizes of the pillars defined by the DWL and the other is a poor lift off process that leaves residues causing the contact area of the top contact and the pillar to be lower than the nominal size.

In order to understand the origin of the problem the same data was plotted taking into account the pillar size (Figure 54). This made clear a relation between the pillar size and the RxA distribution, since higher RxA was found for smaller pillars and higher RxA for larger pillars. This leads us to think that the lift off process of the oxide layer had some issues that left residues thus decreasing the contact area between the pillar and the top contact. This could be an explanation for the dependence of the RxA with the pillar size.

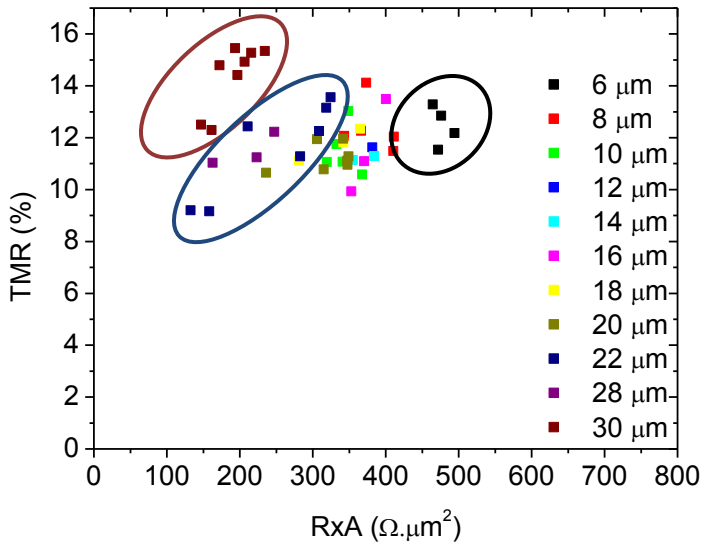

Figure 54 – NO_34 TMR versus RxA plot with pillar size discrimination.

5.2.2.2 CoFeB electrodes annealed for 30 minutes

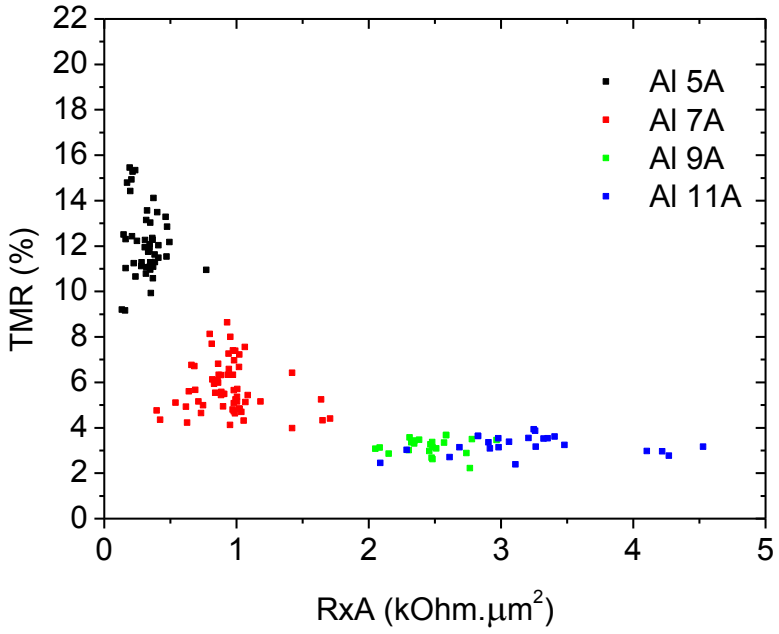

Figure 55 **-** TMR versus RxA for the CoFeB electrode series annealed 30 minutes at 240°C.

Table 10 – Table with the average and standard deviation values for the CoFeB series annealed for 30 minutes

	TMR		RxA (Ω.µm²)	
Al 5 Å	12.10 %	± 1.48	320	± 110
Al 7 Å	5.75 %	± 1.10	940	± 250
Al 9 Å	3.19 %	± 0.35	2460	± 220
Al 11 Å	3.24 %	± 0.41	3210	± 410

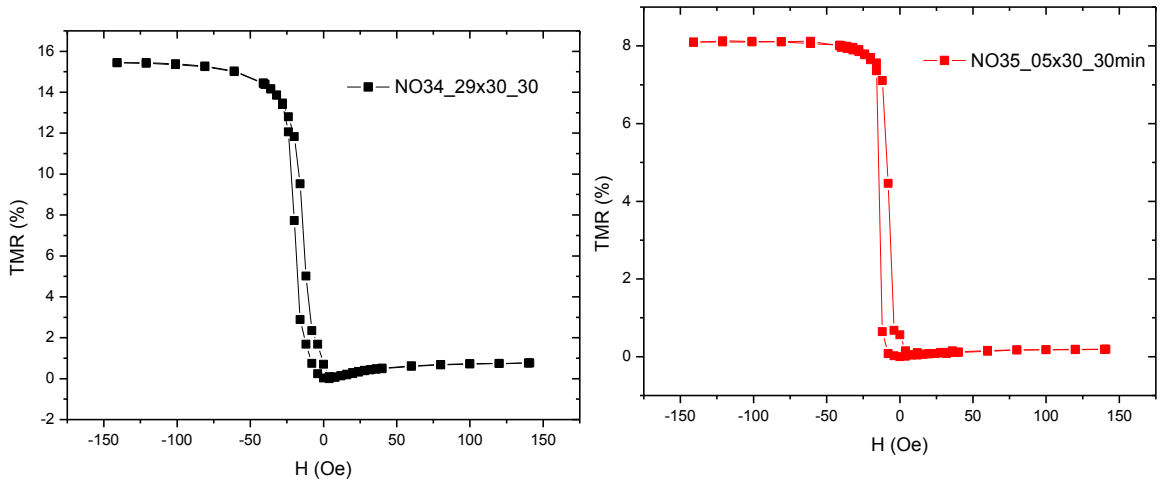

Figure 56 – Example of transfer curves of 900 µm² pillar annealed for 30 minutes from a) Al 5 (NO34); b) Al 7 (NO35)

5.2.2.3 CoFeB electrodes annealed for 60 minutes more

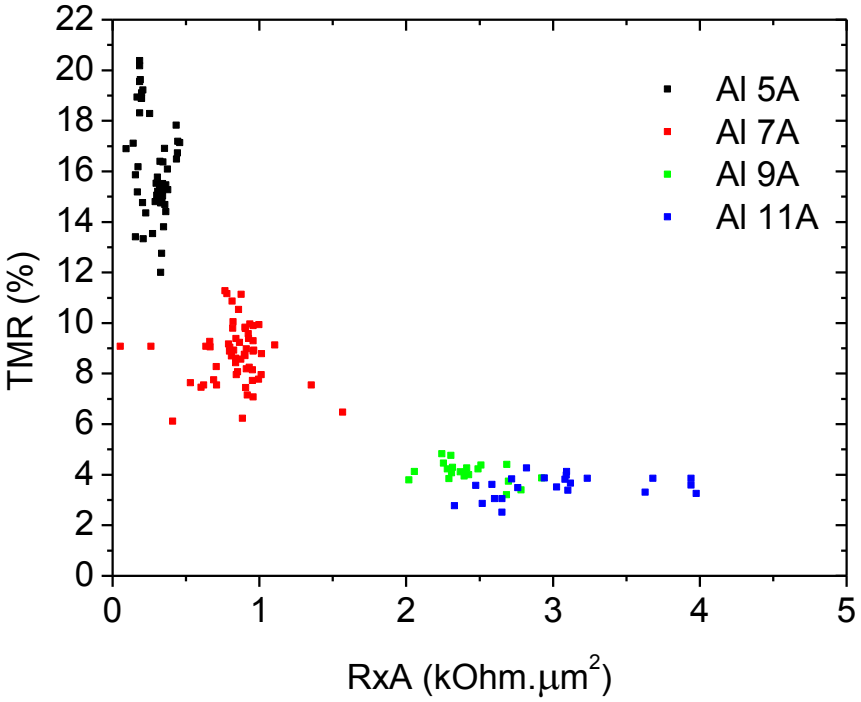

Figure 57 - TMR versus RxA for the CoFeB electrode series annealed 30 + 60 minutes at 240°C.

Table 11 - Table with the average and standard deviation values for the CoFeB series annealed for 30 + 60 minutes at 240°C.

	TMR		RxA (Ω.µm²)	
Al 5 Å	16.1 %	± 1.9	300	± 90
Al 7 Å	8.8 %	± 1.2	800	± 220
Al 9 Å	4.1 %	± 0.4	2400	± 230
Al 11 Å	3.5 %	± 0.5	3040	± 450

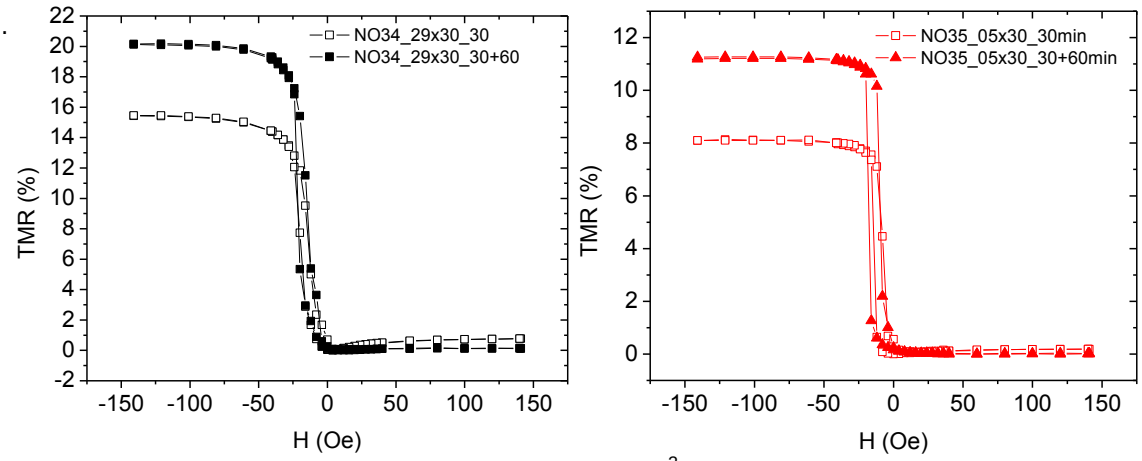

Figure 58 – Comparison of transfer curves of 900 µm² pillar annealed by 30 and by 30 + 60 minutes from a) Al 5 (NO34); b) Al 7 (NO35)

5.2.2.4 CoFe electrode series annealed for 30 minutes

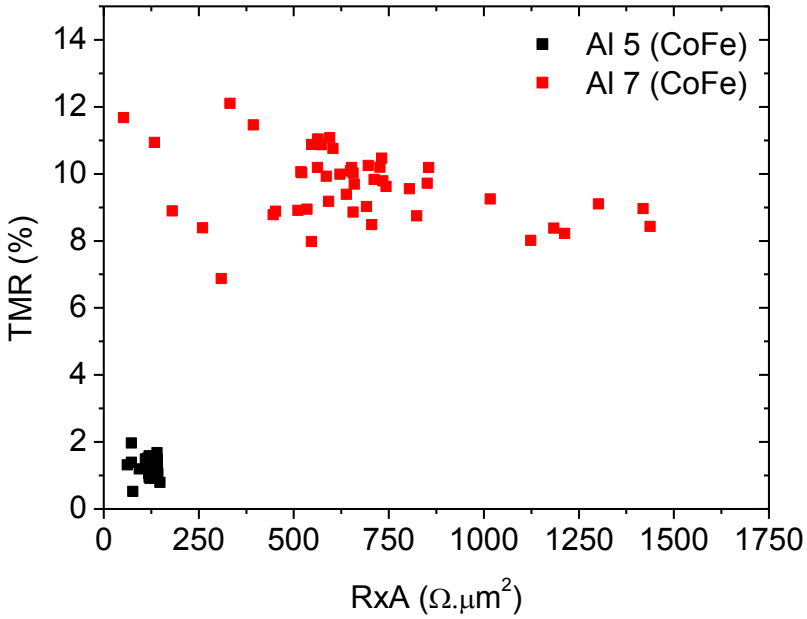

Figure 59 - TMR versus RxA for the CoFe electrode series annealed 30 minutes at 240°C.

Table 12 - Table with the average and standard deviation values for the CoFe series annealed for 30 minutes at 240°C.

	TMR		RxA (Ω.μm²)	
Al 5 Å	1.1 %	± 0.3	122	± 23
Al 7 Å	9.7 %	± 1.1	665	± 291

In this series the samples for 9 Å and 11 Å of Aluminum had a processing problem that increased the Top electrode resistivity. This was resulted in transfer curves from where no reliable TMR or RxA values could have been extracted.

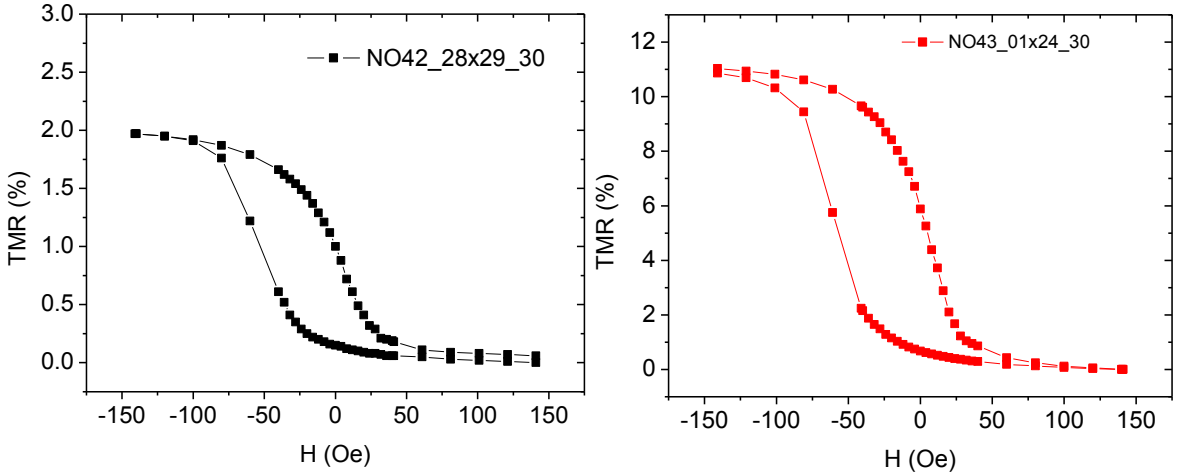

Figure 60 – Comparison of transfer curves for with CoFe electrodes annealed 30 minutes from a) Al 5 (NO42); b) Al 7 (NO43)

5.2.2.5 CoFe electrode series annealed for 60 minutes more

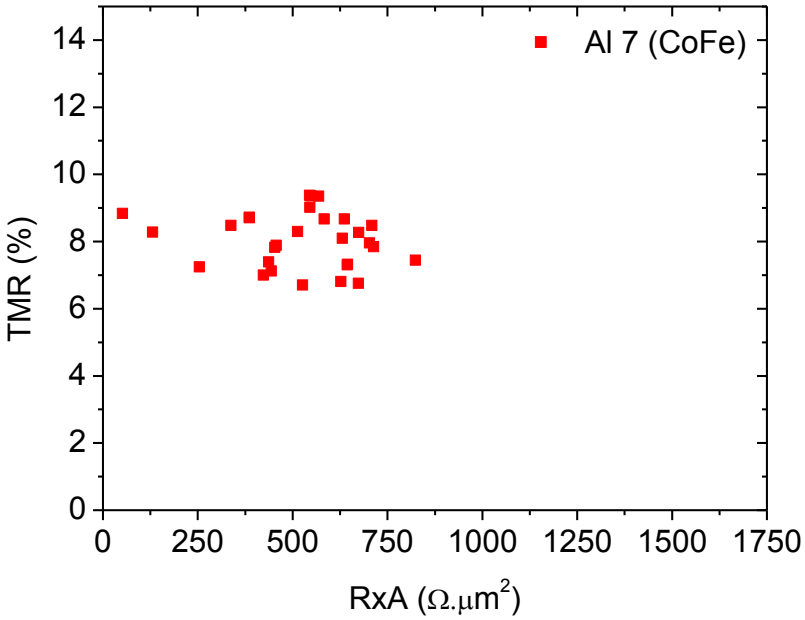

Figure 61 - TMR versus RxA for the CoFe electrode series annealed 30 + 60 minutes at 240°C.

Table 13 - Table with the average and standard deviation values for the TMR and RxA of CoFe Al 7 Å annealed for 30 + 60 minutes at 240°C.

	TMR		RxA (Ω.μm²)	
Al 7 Å	8.1 %	± 0.8	520	± 176

For the 5 Å layer the transfer curves the extra 60 min annealing had clear impact on the transfer curve.

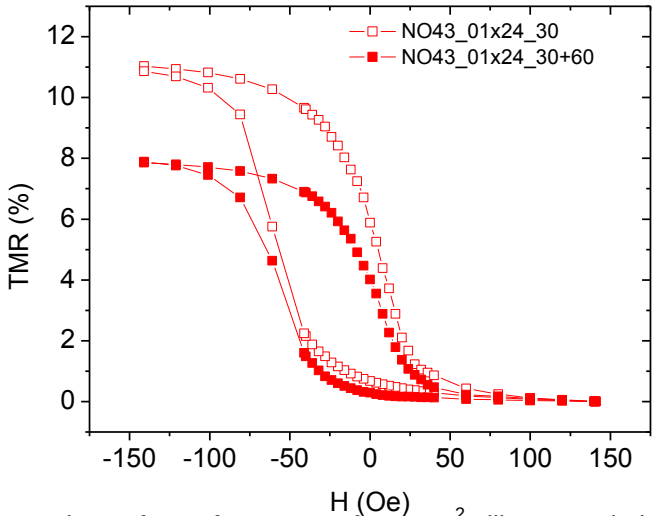

Figure 62 – Comparison of transfer curves of 576 μm² pillar annealed by 30 and by 30 + 60 minutes from Al 7 (NO43).

5.2.3 Discussion

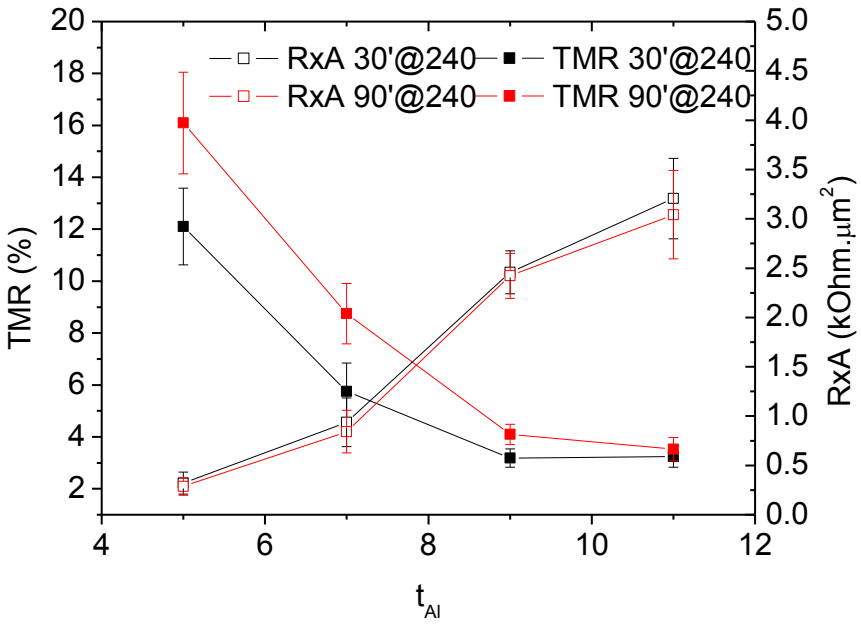

Figure 63 – TMR(black) and RxA (red) values as a function of thickness of pure aluminum. The ■ show the results for the 30 minutes annealing. The ▲ represent the values of the 30+60 minutes annealing. The error bars are obtained from the standard deviation of the clusters shown in the TMR vs RxA graphics.

The experimental results provide clear evidences that the thickness of Al, the electrodes and the annealing time are important process variables for the Natural Oxidation technique.

From Figure 63, a clear decrease of TMR with the thickness of the Al layer. This is related to tunneling properties with the oxidation, for lower thicknesses the tunneling properties appears to be better since the oxidation degree is also higher. The annealing time also has an impact on the TMR value. A comparison of the averages of TMR and RxA between the 30 minutes and 30+60 minutes annealing is presented in Figure 63.

The oxidation of the Al film occurs with the exposition of the film to the atmosphere. HRTEM profiles clearly show that the oxidized regions develop in direction normal to the barrier plane. Low oxidation result in discrete non oxide islands, while further oxidation leads to a continuous barrier. The post-deposition annealing leads to the diffusion of oxygen causing the islands to expand and thus decreasing the non oxide islands sizes. [34]

These assumptions allow us to understand the behavior observed in our experimental study. Assuming the decrease of TMR is due to under oxidized barrier the barrier is composed by AlOx islands and pure aluminum. The existence of pure aluminum islands will reduce the tunneling properties of the barrier and thus a lower TMR is observed. This also justifies the increase of TMR with the annealing since the annealing will promote the diffusion of oxygen and thus create a more uniform barrier.

The RxA has a exponential relation with the barrier thickness, thus it was expected that the lowest RxA corresponded to the lowest barrier thickness. However the evolution of RxA with thickness (Figure 63) is not increasing exponentially, because all the barriers have different ratio between the AlOx islands and pure aluminum. This means that even though the barrier is thicker the insulating properties are lower thus lower resistivity. This in agreement with the under oxidation assumption, since the oxidation time is the same but the penetration depth of the oxidation is lower.

The electrodes also show to have a very important role in the TMR ratio. For the CoFe series even though only two samples could be measured a completely different relation between the Al 5 and Al 7 samples was observed. For the Al 5 the CoFeB electrodes a TMR of 12% and an RxA of 300 $\Omega.\mu m^2$ were measured while for the CoFe electrodes a TMR of only1.5% and an RxA of 150 $\Omega.\mu m^2$.

With the aluminum oxide barrier mechanism described by Cerezo [34] and the Magnetic Dead Layer study presented in chapter 4 the results were expected.

Cerezos' study indicates that due to the crystallographic texture of the CoFe a considerable grain boundary grooving leading to a rough, wavy surface onto which Al is deposited. Since a limited thickness of Al was deposited and might not be enough to fill the grooves at the grain boundaries therefore probably only partially cover the CoFe surface.

In this case the relation between the roughness and Al thickness deposited was enough to produce a continuous barrier. This is supported by the VSM, since the Stack shows a Free Layer.

From the MLD study a clear relation from the annealing and the saturation magnetization was observed and the oxygen diffusion was found to be the major cause for the decrease in magnetic moment of the CoFe layers.

The difference of the Al 5 Å barrier behavior with the CoFeB and CoFe electrodes could be justified due to the behavior shown by the electrodes in the MDL study. Since the barrier thickness is very low over oxidation can be occurring and this would result in the oxidation and an increase in magnetic layers of the CoFe and thus a decrease of the TMR value. On the other hand the magnetization saturation of CoFeB did not show a dependence on the oxygen diffusion. This could be related to the results in TMR since the barrier can be over oxidized resulting in the oxidation of the CoFe electrode, while CoFeB is not sensitive to the oxidation.

The RxA on the CoFe electrode sample is lower which can be due to the different resistivity of the electrodes, since the CoFe has lower resistivity than CoFeB. The resistivity increases with the Boron content mostly due to the increasing percentage of amorphous phase. [35]

6 Conclusions

This thesis has focused the optimization of thin films based in CoFeB-AlOx for integration in advanced Magnetoresistive devices. Magnetoresistive devices require a pinned a free layer and a barrier in order to show the Magnetoresistive effect.

In this thesis a pinned layer with an exchange of 1000 Oe was obtain with combined exchange bias with a MnIr/CoFe system and a SAF with CoFe/Ru/CoFeB sandwich. In order to obtain an AFM/FM exchange bias, several seed layers where used and their influence on the MnIr/CoFe exchange bias and coercivity was discussed. The roughness of the Bottom Electrode was related with coercivity and the crystallographic phase of the seed layer to the exchange bias of the MnIr/CoFe system, since the (111) crystallographic orientation of the MnIr is a requirement. A Ru 50 Å seed layer showed to be promote a reasonable MnIr growth and a 300 Oe exchange bias and a 19 Oe coercivity was reported.

A Dead Layer study was performed in order to determine the influence of annealing in the CoFe/AlOx and CoFeB/AlOx interfaces. A reduction of the thickness of dead layers was observed for the CoFeB, while the CoFe shown the opposite behavior. Through this method two interesting phenomenon can be observed. For the CoFe layer with 15 Å a ferromagnetic (as deposited) to paramagnetic (300°C) phase transition was observed. However the opposite behavior was observed for the layers of CoFeB with 10 Å. The main reason for this behavior is the presence of boron in the CoFeB alloys.

For the MTJ stacks produced by Natural Oxidation high dependence of the Aluminum layer thickness was found. An optimal thickness with of 5 Å with 30 minutes of Natural Oxidation showed a TMR response of 20% and an RxA 180 $\Omega.\mu m^2$ for CoFeB electrodes.

The annealing time was also found to be a determinant parameter in the TMR value since it had a 4% increase on the CoFeB electrodes with an additional 60 minutes annealing time.

On the other hand the CoFe showed better results with a 7 Å with only 12% of TMR and and RxA of 50 $\Omega.\mu m^2$. The Al 5 Å was proven to be too thin and with a 30 minute oxidation time the CoFe electrode suffered oxidation resulting in poor values of TMR.

The CoFeB alloys are a better choice for Natural Oxidation technique since it allows a better oxidation degree of the barrier resulting in better values of TMR.

7 Bibliography

[1] A. E. Berkowitz and K. Takano, "Exchange anisotropy - a review," *J. Magn. Magn. Mater.,* 1999.

[2] J. Nogues and I. K. Schuller, "Exchange bias," *J. Magn. Magn. Mater,* 1999.

[3] R. L. Stamps, "Mechanisms for exchange bias," *J. Phys. D: Appl. Phys,* 2000.

[4] K. Takano, R. H. Kodama, A. E. Berkowitz, W. Cao and G. Thomas, "Interfacial uncompensated antiferromagnetic spins: Role in unidirectional anisotropy in polycrystalline NiFe/CoO bilayers," *Phys. Rev. Lett.,* 1997.

[5] M. Julliere, "Tunneling between ferromagnetic films," *Physics Letters A,* vol. 54A, no. 3, pp. 225-226, 1975.

[6] J. Moodera, L. R. Kinder, T. M. Wong and R. Meservey, "Large Magnetoresistance at Room Temperature in Ferromagnetic Thin Film Tunnel Junctions," *Physical Review Letter,* vol. 74, no. 16, pp. 3273-3276, 1995.

[7] D. Wang, J. M. D. C. Nordman, Z. Qian and J. Fink, "70% TMR at Room Temperature for SDT Sandwich Junctions with CoFeB as Free and Reference Layers," *IEEE Transactoins on Magnetics,* 2004.

[8] R. Waser, Nanoelectroniscs and Information Technology, Wiley-VHC, 2012.

[9] S. Yuasa and D. Djayaprawira, "Giant tunnel magnetoresistance in magnetic tunnel junctions with a crystalline MgO(001) barrier," *J. Phys. D: Appl. Phys ,* vol. 40, pp. R337-R354, 2007.

[10] J. M. E. Harper, "Thin Film Processes," in *Part II-5 Ion Beam Deposition*, New York, Academic Press, INC., 1978, pp. 175-208.

[11] R. Ferreira, "Ion Beam Deposited Magnetic Spin Tunnel Junctions targeting HDD Read Heads, Non-Volatile Memories and Magnetic Field Sensor Applications," Universidade Técnica de Lisboa, 2008.

[12] N. P. Barradas and C. Jeynes, "Advanced physics and algorithms in the IBA DataFurnace," *Nucl. Instrum. and Meth. B,* 2008.

[13] J. W. D. Callister, Materials Science and Engineering, John Wiley & Sons, Inc., 2007.

[14] G. Herzer, "Grain size dependence of coercivity and permeability in nanocrystalline ferromagnets," *IEEE Trans. Magn.,* vol. 26, no. 9, pp. 1397-1402, 1997.

[15] S. Cardoso, C. Cavaco, R. Ferreira, L. Pereira, M. Rickart, P. P. Freitas, N. Franco, J. Gouveia and N. P. Barradas, "Characterization of CoFeB electrodes for tunnel junctions," *Journal of Applied Physics,* vol. 97, no. 10C916, 2005.

[16] Y.-T. Chen and S. M. Xie, "Magnetic and Electric Properties of Amorphous Co40Fe40B20 Thin Films," *Journal of Nanomaterials,* vol. 2012, no. 486284, 2011.

[17] T. Kubota, T. Daibou, M. Oogane, Y. Ando and T. Miyazaki, "Tunneling Spin Polarization and Magnetic Properties of Co-Fe-B Alloys and Their Dependence on Boron Content," *Japanese Journal of Applied Physics,* vol. 46, no. 11, pp. L250-L252, 2007.

[18] D. Watanabe, M. Oogane and S. Mizukami, "Boron Composition Dependence of Spin-Transfer Switching in Magnetic Tunnel Junctions with CoFeB Free Layers," *Japanese Journal of Applied Physics,* vol. 48, no. 013001, 2009.

[19] A. Veloso, "Advanced spin valve read heads for recording densities towards 100 Gbit/in2," Universidade Técnica de Lisboa, Lisboa, 2001.

[20] M. Rickart, A. Guedes, J. Ventura, J. B. Sousa and P. P. Freitas, "Blocking temperature in exchange coupled MnPt/CoFe bilayers and synthetic antiferromagnets," *Journal of Applied Physics,* vol. 97, no. 10K110, 2005.

[21] A. J. Devasahayam and M. H. Kryder, "The dependence of the antiferromagnet/ferromagnet blocking temperature on antiferromagnet thickness and deposition conditions," *Journal of Applied Physics,* 1999.

[22] J. v. Driel, K.-M. H. L. F. R. Boer and R. Coehoom, "Exchange biasing by Ir19Mn81: Dependence on temperature, microstructure and antiferromagnetic layer thickness," *J. Appl. Phys.,* 2000.

[23] M. Pakala, H. Huai, G. Anderson and L. Miloslavsky, "Effect of underlayer roughness, grain size, and crystal texture on exchange coupled IrMn/CoFe thin films," *Journal of Applied Physics,* 2000.

[24] N. P. Aley and K. O'Grady, "Compositional dependence of antiferromagnetic anisotropy in IrMn/CoFe exchange bias systems," *Journal of Applied Physics,* 2011.

[25] D. N. H. Nam, W. Chen, K. G. West, D. M. Kirkwood, J. Lu and S. A. Wolf, "Propagation of Exchange Bias in CoFe/FeMn/CoFe Trilayers," University of Virginia, 2013.

[26] V. K. Sankaranarayanan, S. M. Toon, C. G. Kim and C. Kim, "Exchange bias variations of the seed and top NiFe layers in NiFe/FeMn/NiFe trilayer as a function of seed layer thickness," *Journal of Magnetism and Magnetic Materials,* 2005.

[27] H. Fulara, S. Chaudhary and D. K. Pandya, "Positive exchange bias in as-deposited ion-beam sputtered," J. Appl. Phys, 2011.

[28] M. D. Stiles, "Interlayer exchange coupling," *Concepts Condens. Mat. Phys.,* 2005.

[29] J. Yu, D. Kent and S. S. P. Parkin, "Exchange biasing in polycrystalline thin film microstructures," *Journal of Applied Phisics,* 2000.

[30] W. Raberg and A. Gupta, "Materials Requirements for Magnetic Random-Access Memory (MRAM) Devices," in *Thin Films and Heterostructures for Oxide Electronics*, Springer, 2005, pp. 129-151.

[31] J. Wang, Y. Liu, P. P. Freitas, E. Snoeck and J. L. Martins, "Continuos thin barriers for low-resistance spin-dependent tunnel junctions," *Journal of Applied Physics,* vol. 93, no. 10, p. 8367, 2003.

[32] K. S. Moon, Y. Chen and Y. Huai, "PtMn-based spin dependent tunneling materials with thin alumina barrier fabricated by two-step natural oxidation.," *J. Appl. Phys.,* vol. 7967, no. 2002, p. 7965, 2002.

[33] A. Augusto, "Optimization of the etching parameters of the ion milling system Nordiko 3600," Universidade Técnica de Lisboa, Lisbon, 2007.

[34] A. Cerezo, A. K. Perford-Long, D. J. Larson, S. Pinitsoontorn and E. W. Singleton, "The formation mechanism of aluminum oxide tunnel barriers," *J Mater Dci,* vol. 41, pp. 7843-7852, 2006.

[35] M. Munakata, S.-I. Aoqui and M. Yagi, "B-Concentration Dependence on Anisotropy Field of CoFeB Thin Film for Gigahertz Frequency Use," *IEEE Transaction on Magnetics,* vol. 41, no. 10, pp. 3262-3265, 2005.

[36] J. Coey, Magnetism and Magnetic Materials, Cambridge University Press, 2009.

[37] I. F. J. a. D. S. S. Zutic, "Spintronics: Fundamentals and applications," *REVIEWS OF MODERN PHYSICS,* pp. 323-410, 23 April 2004.

[38] Z. e. a. Qian, "Effective anisotropy field in the free layer of patterned spin-valve resistors," *JOURNAL OF APPLIED PHYSICS,* 17 May 2011.

[39] J. M. D. Coey, "Materials for Spin Electronics," in *Spin Electronics (Lecture Notes in Physics)*, Berlin Heidelberg, Springer-Verlag, 2001, p. pp. 277–297.

[40] J. v. Driel, R. Coehoorn, K., M. H. Lenssen, A. E. T. Kuiper and F. R. d. Boer, "Thermal stability of Ir–Mn as exchange biasing material," *Journal of Applied Physics,* 1999.

[41] C. Leighton, "Thickness-dependent coercive mechanisms in exchange-biased bilayers," *PHYSICAL REVIEW B,* 2002.

[42] C. Leighton, J. Nogués, B. J. Jönsson-Åkerman and I. K. Schuller, "Coercivity Enhancement in Exchange Biased Systems Driven," *Physical Review Letters,* 2000.

[43] Z. Li and S. Zhang, "Coercive mechanisms in ferromagnetic-antiferromagnetic bilayers," *Physical Review B,* 2000.

[44] H. N. Fuke, K. Saito, Y. Kamiguchi, H. Iwasaki and M. Sahashi, "Spin-valve giant magnetoresistive films with antiferromagnetic Ir-Mn layers," *Journal of Applied Physics,* 1997.

[45] G. Vallejo-Fernandez, N. P. Aley, L. E. Fernandez-Outon and K. O'Grady, "Control of the setting process in CoFe/IrMn exchange bias systems," *Journal of Applied Physics,* 2008.

[46] M. Mao, S. Funada, T. S. M. M. H.-C. T. C. Q. C-Y. Hung and L. Miloslavsky, "Enhanced exchange biasing in ion-beam sputtered bottom spin-valve films," *IEEE Transactions on Magnetics,* 1999.

[47] L. E. Fernandez-Outon, G. Vallejo-Fernandez, S. Manzoor and K. O'Grady, "Thermal instabilities in exchange biased materials," *Journal of Magnetism and Magnetic Materials,* 2006.

[48] H. Tsuge and T. Mitsuzuka, "Magnetic tunnel junctions with in-situ naturally-oxidized tunnel barrier," *Appl. Phys. Lett.,* vol. 71, no. 3296, 1997.

[49] K. Matsuda, A. Kamijo, T. Mitsuzuka and H. Tsuge, "Exchange biased magnetic tunnel junctions fabricated in-situ natural oxidation," *J. Appl. Phys.,* vol. 85, pp. 5261-5263, 1999.

[50] Y. Xu, E. Kernohan, D. Freeland, A. Ercole, M. Tselepi and J. Bland, "Evolution of the ferromagnetic phase of ultrathin Fe films grown on GaAs (100)," *Physical Review B,* vol. 58, no. 2, pp. 890-896, 1998.

[51] H. Boeve, J. d. Boeck and G. Borghs, "Low-resistance magnetic tunnel junctions by in-situ natural oxidation," *J. Appl. Phys.,* vol. 89, pp. 482-487, 2001.

[52] A. T. A. Wee, S. X. Wang and K. Sin, "In-situ characterization of oxide growth for fabrication

spin-dependent tunnel junctions," *IEEE Trans. on Magn.,* vol. 35, pp. 2949-2951, 1999.

[53] M. F. Gillies, W. Oepts, A. E. T. Kuiper and R. Coehoorn, "The optimum oxidation state of AlOx magnetic tunnel.," *IEEE Trans. Mag.,* vol. 35, pp. 29991-2993, 1999.

[54] J. Das, "Magnetic Random Access Memories: Technology assesment & tunnel barriel reliability study," Katholieke Universiteit Leuven, 2006.

[55] E. Y. Chen, R. Whig, J. M. Slaughter, D. Cronk, J. Goggin, G. Steiner and S. Tehrani, "Comparison of oxidation methods for magnetic tunnel juntion material," *J. Appl. Phys,* vol. 87, pp. 6061-6063, 2000.

8 Appendix

8.1 Appendix A – Runsheet

STEP 0 – Clean Glass Substrate (2.5 cm × 2.5 cm)

Machine: **Wet Bench (Ultrasound)** Date: __/__/____

Conditions: Clean for 30 minutes in Alconox solution with ultrasound;

Clean with DI water and blow dry with compressed air gun.

STEP 1 – Tunnel Junction deposition

Machine: **Nordiko 3600 (IBD)** Date: __/__/____

Sample # N36TJ_NO_34	**Structure**
Top Contact	CoFeB 40/Ru 100
Barrier	Al 5 + 30 minutes of in situ Natural Oxidation
SAF	CoFe 30 /Ru 9.2 / CoFeB 30
Antiferromagnet	Ru 50/MnIr 180
Bottom Contact	[Ru 150/NiFeCr 50]x2

STEP 2 – 1st Lithography: Junction stack definition

Machine: **DWL** Date: __/__/____

Conditions: a) **Coating PR**: - Vapour prime 30'

- Coat 1.5 µm PR (recipe 6/2)

b) **Exposure**: - Mask: **SKMN_MTJBE (on /h2)**

- Map: **AMSION**

- Origin: X = 3500 Y = 3500

- Energy: _____ % Focus: _____

c) **Developing**: - Recipe 6/2

Development time: 60 s

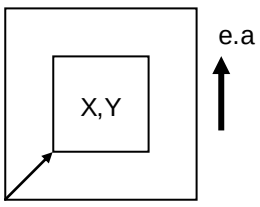

Align Marks Coordinates	1	2	3	4	5	6
X	250	17750	250	17750	250	17750
Y	250	250	6750	6750	13750	13750

STEP 3 – 1st Ion Milling: Bottom electrode definition

Machine: **Nordiko 3600 (IBD)** Date: __/__/____

Assist Gun	*RF Power*	*V+*	*I+*	*V-*	*Ar Flow*	*Pressure*
Setpoint Reading	150-200W	735V	+105 mA	-350V	10 sccm	1 x 10^{-4} Torr

Substrate Table	*Rotation*	*Angle*	*Time*
Setpoint Reading	30 rpm	60 deg	Full stack thickness (_____Å)

STEP 4 – Resist strip

Machine: **Wet bench** Date: __/__/____

Conditions: **a) To strip**: Place in ***microstrip 3001*** at 65ºC;

Apply several steps of 10 minute of ***ultrasounds***.

b) To clean: Rinse with ***IPA*** then with ***DI water***;

Blow dry with ***compressed air gun***.

Total time in hot microstrip: _____ Ultrasounds time: _____

Optical inspection:

STEP 5 – 2nd Lithography: Top electrode and junction definition

Machine: **DWL** Date: __/__/____

Conditions: a) **Coating PR**: - Vapour prime 30'

- Coat 1.5 µm PR (recipe 6/2)

b) **Exposure**: - Mask: **SKMN_MTJPL**

- Map: **AMSION**

- X-align = _____ Y-align = _____

- Energy: _____ % Focus: _____

c) **Developing**: - Recipe 6/2

- Development time: _____

STEP 6 – 1st Ion Milling: Junction stack definition

Machine: **Nordiko 3600 (IBD)** Date: __/__/____

Assist Gun	*RF Power*	*V+*	*I+*	*V-*	*Ar Flow*	*Pressure*
Setpoint Reading	150-200W	735V	+105 mA	-350V	10 sccm	1 x 10^{-4} Torr

Substrate Table	*Rotation*
Setpoint Reading	30 rpm

STEP 6.1 – 60 deg etching

Etching rate: ~ 1 Å/s Etching thickness: Top Contact (_____ Å) + Barrier (____ Å)

Etching time: _____ s

STEP 6.2 – 30 deg etching

Etching rate: ~ 1 Å/s Etching thickness: SAF (_____ Å) + 0.5 x Antiferromagnet (_____ Å)

Etching time: _____ s

STEP 7 – Insulating layer deposition (1000Å)

Machine: **UHVII** Date: __/__/____

Conditions:

UHV II	*RF Power*	*Pressure*	*Gas Flow*	*Deposition Rate*
Al_2O_3 Deposition	200W	2.0 mTorr	4 sccm	~ 11 A/min

B.P. =_____Torr Deposition started @ _____

Deposition finished @ _____

STEP 8 – Insulator lift-off

Machine: **Wet bench** Date: __/__/____

Conditions: **a) To strip**: Place in ***microstrip 3001*** at 65ºC; ***with ultrasounds***.

b) To clean: Rinse with ***IPA*** then with ***DI water***;

Blow dry with ***compressed air gun***.

Total time in hot microstrip: _____ Ultrasounds time: _____

Optical inspection:

STEP 9 – 3rd Lithography: Contact and top electrode definition

Machine: **DWL** Date: __/__/____

Conditions: a) **Coating PR**: - Vapour prime 30'

- Coat 1.5 µm PR (recipe 6/2)

b) **Exposure**: - Mask: **SKMN_MTJTE**

- Map: **AMSION**

- X-align = _____ Y-align = _____

- Energy: _____ % Focus: _____

c) **Developing**: - Recipe 6/2

- Development time: _____

Comments:

STEP 10 – Contact lead deposition

Machine: **N7000** B.P.(mod.2)= _____ T cryo = _____

B.P.(mod.3)= _____ T cryo = _____

B.P.(mod.4)= _____ T cryo = _____

Run #_____

Seq.48 (svpad) –

mod.2 – f.9 (40'' soft sputter etch) P=60W/40W, p=3mTorr, 50 sccm Ar

mod.4 – f.1 (3000A Al, 1'20'') P=2 kW, 3mTorr, 50 sccm Ar

mod.3 - f.19 (150A $TiWN_2$, 27'') 0.5 kW, 3mTorr, 50 sccm Ar + 10sccm N_2

STEP 11 – Metal lift-off

Machine: **Wet bench** Date: __/__/____

Conditions: **a) To strip**: Place in ***microstrip 3001*** at 65°C;with ***ultrasounds***.

b) To clean: Rinse with ***IPA*** then with ***DI water***;

Blow dry with ***compressed air gun***.

Total time in hot microstrip: _____ Ultrasounds time: _____

Optical inspection:

STEP 12 – Annealing

Machine: **Annealing setup** Date: __/__/____

Conditions:

Time: 30 minutes B.P. = _____ Torr

Temperature: 240 °C Time to push to magnet: _____

Heat rate: 5 °C/min.

8.2 Appendix B – Mask

The Mask used to perform the measurements presented in this thesis is composed of 225 MTJ pillars. The pillar shape are squares from 2 to 30 μm in side (4 to 900 μm^2).

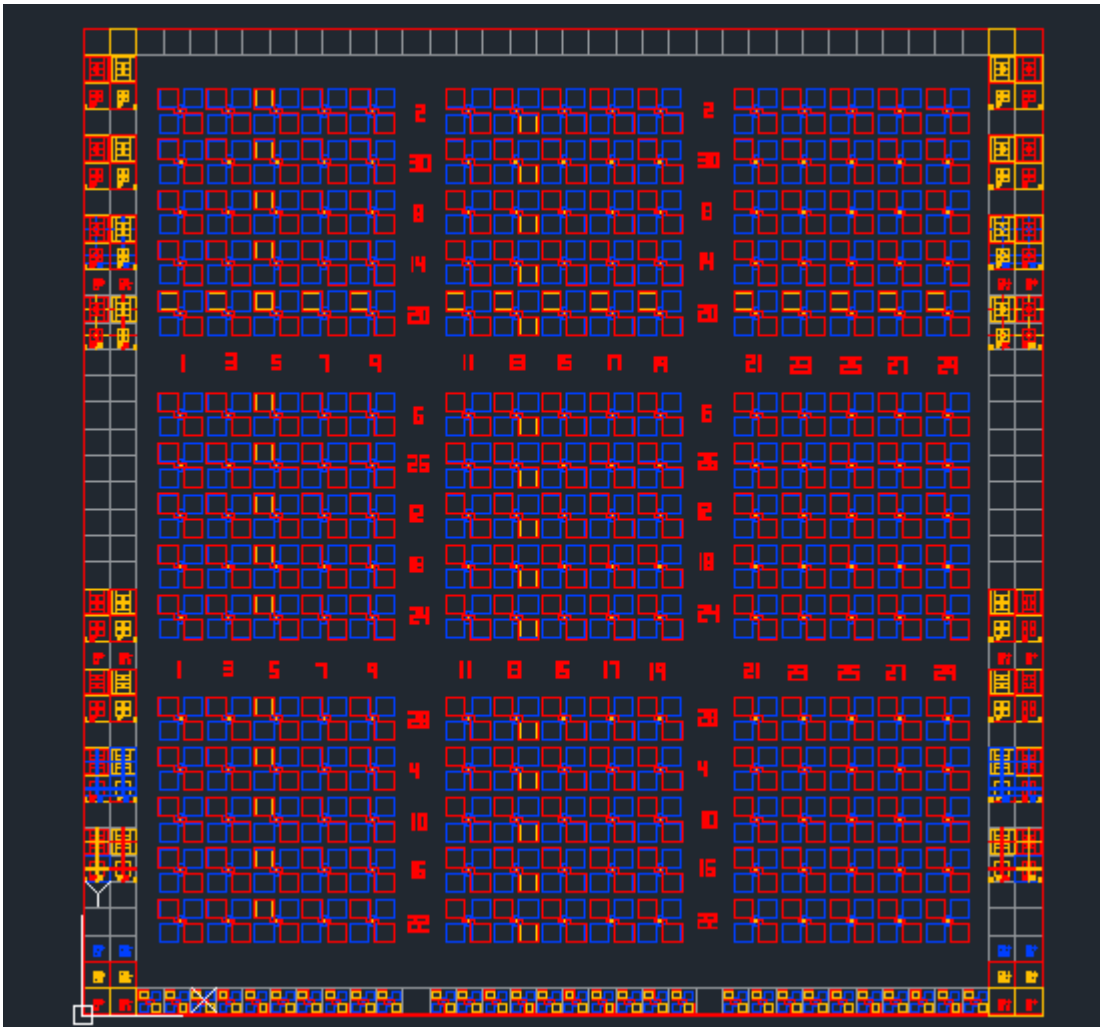

In each line (pair numbers) there are 15 pillars of the same size. The size matches the number of the line. Odd numbers were used to identify the column.

On the corners cross structures are present in order to perform the alignment of the mask.

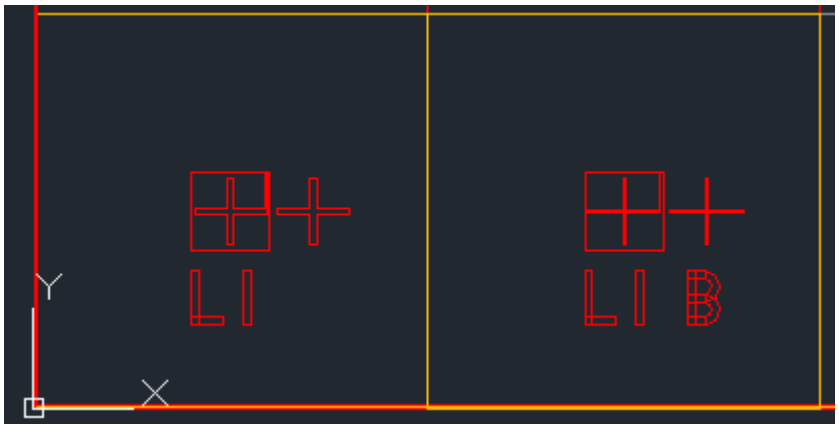

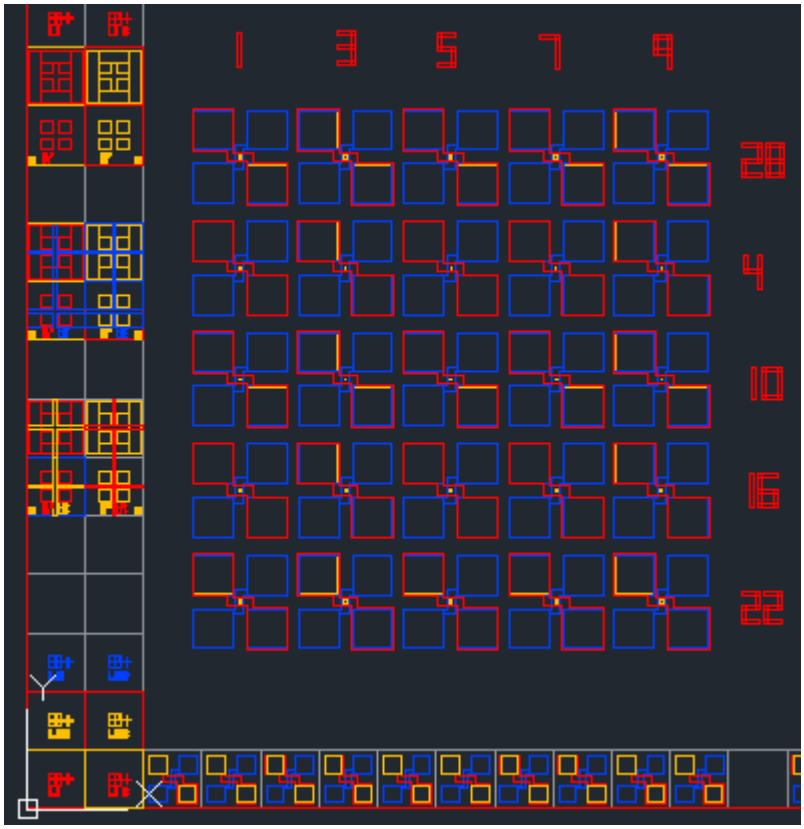

8.2.1 MTJ_SKMNBE

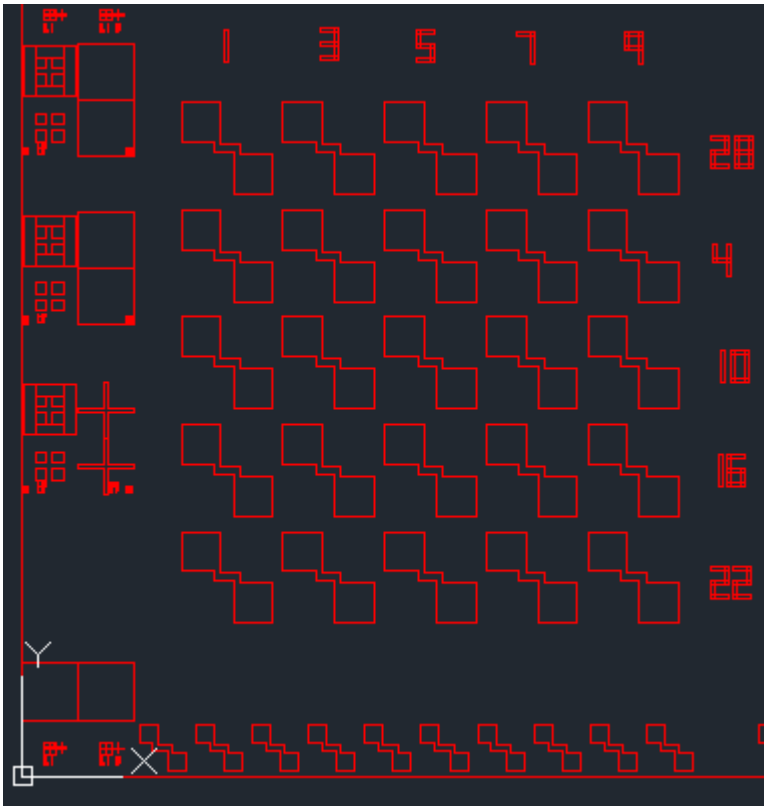

8.2.2 MTJ_SKMNPL

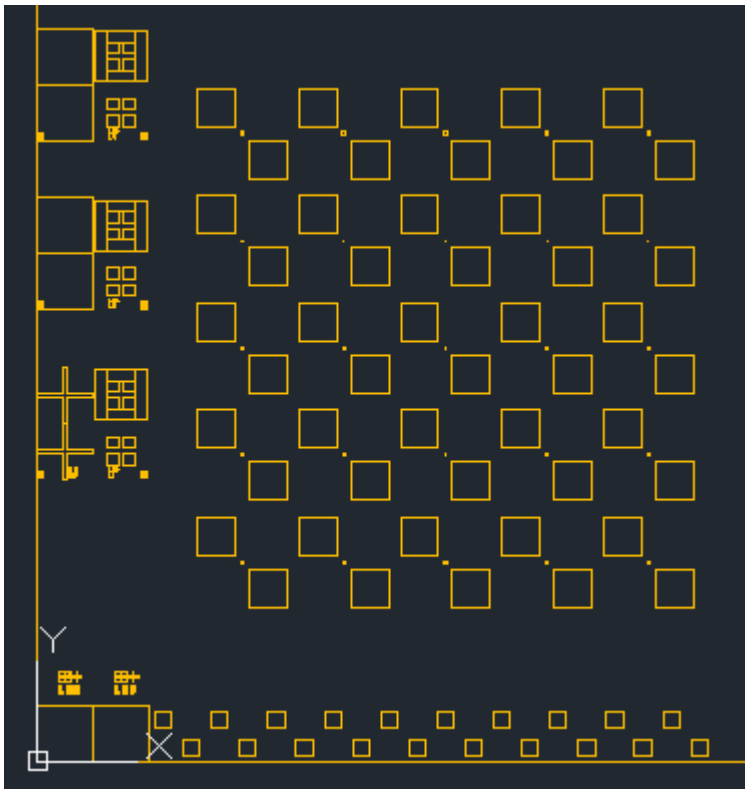

8.2.3 MTJ_SKMNTE